

QUANTUM CONFINEMENT IN
SILICON CLATHRATE
QUANTUM DOTS

by
Nicholas P. Brawand

© Copyright by Nicholas P. Brawand, 2013

All Rights Reserved

A thesis submitted to the Faculty and the Board of Trustees of the Colorado School of Mines in partial fulfillment of the requirements for the degree of Master of Science (Applied Physics).

Golden, Colorado

Date _____

Signed: _____

Nicholas P. Brawand

Signed: _____

Mark T. Lusk
Thesis Advisor

Golden, Colorado

Date _____

Signed: _____

Thomas E. Furtak
Professor and Head
Department of Physics

ABSTRACT

The relationship between crystal structure and quantum confinement is quantified by computationally analyzing sets of silicon quantum dots associated with nine types of clathrates. Density functional theory is used to show that bulk energy gap between the highest occupied and lowest unoccupied Kohn-Sham orbitals varies by more than 1 eV, both above and below that of diamond silicon. The approach is also used to relate dot size to energy gap to identify a linear correlation between quantum confinement sensitivity and bulk-crystal effective mass. All clathrates are found to have a confinement sensitivity less than that of diamond silicon. Bulk properties (gap and effective mass) can therefore be used to identify clathrate semiconductors with promising optoelectronic properties. For example, the combined gap and confinement sensitivity of Type VII clathrate results in a low energy gap for quantum dots within 1 to 2 nm in diameter, making type VII worthy of consideration for efficient multiple exciton generation and other optoelectronic applications.

TABLE OF CONTENTS

ABSTRACT	iii
LIST OF FIGURES	vii
LIST OF TABLES	viii
LIST OF SYMBOLS	ix
LIST OF ABBREVIATIONS	x
ACKNOWLEDGMENTS	xi
DEDICATION	xii
CHAPTER 1 INTRODUCTION	1
1.1 Background	1
1.1.1 High Pressure Phases	2
1.1.2 Clathrates	2
CHAPTER 2 COMPUTATIONAL METHODS	5
2.1 Density Functional Theory	5
2.1.1 Motivation: Riding The Wave Function	6
2.1.2 It's All About the Density	7
2.1.3 Putting It All Together	10
2.2 The Exchange and Correlation Energy of Jelly	11
2.2.1 Background Information	11
2.2.1.1 The State of the Vacuum	13
2.2.1.2 Some Operators Carpool, Some Do Not	14

2.2.1.3	Operators of Operators	14
2.2.2	A Positive Background	15
2.3	The Exchange-Correlation Functional	17
2.3.1	LDA	17
2.3.2	Other Functionals	18
2.4	Geometry Optimization	20
2.4.1	The Conjugate Gradient Method	20
2.4.2	Relaxation in DFT	21
2.5	Methodology	21
2.5.1	The Software Packages	22
2.5.2	Constraints and Parameters	22
CHAPTER 3 PROPERTIES OF BULK CLATHRATES		24
3.1	Structural Properties	24
3.1.1	Clathrates	24
3.1.2	Other Silicon Allotropes	25
3.2	Electronic	26
3.2.1	Electronic Band Structures of The Silicon Clathrates	26
3.2.2	Calculated Dielectric Constants for The Silicon Clathrates	26
3.2.3	Electronic Band Structures of The Other Silicon Allotropes	28
3.3	Effective Masses	28
3.3.1	Methodology	29
3.3.2	Effective Mass Results	30
3.3.3	Comparison With Literature	30

CHAPTER 4 CLATHRATE QUANTUM DOTS	35
4.1 Quantum Dot Structures	35
4.1.1 Relaxed Clathrate Quantum Dot Structures	35
4.1.2 Un-relaxed Quantum Dot Structures	36
4.2 Spatial Confinement of the HOMO/LUMO Gap	36
4.2.1 HOMO/LUMO Gap	37
CHAPTER 5 EFFECTIVE MASS AND QUANTUM CONFINEMENT	43
5.1 Theory	43
5.2 Comparison Between the Confinement Constant and Effective Mass	47
CHAPTER 6 DISCUSSION AND CONCLUSION	49
REFERENCES CITED	53
APPENDIX - COMPUTATIONAL DETAILS CONTINUED	58
A.1 KGridCutOff	58

LIST OF FIGURES

Figure 2.1	Jacob’s ladder of exchange-correlation functionals. Taken from	19
Figure 3.1	The geometry of type VII clathrate.	25
Figure 3.2	The geometry of clathrate structures I, II, III, IV, V, VI,VII, VIII, and H. . .	26
Figure 3.3	The energy per atom relative to diamond silicon for clathrates type I-VIII, H and seven other silicon allotropes. (L-R) clathrate types 1-8, H, non-clathrate Si allotropes BCT, III, diamond, IV, M4, T12, wurtzite, and XII.	28
Figure 3.4	The calculated electronic band structures of silicon clathrates type I-VIII and type H.	32
Figure 3.5	The calculated electronic band structures of silicon allotropes I, XII, T12, and Wurtzite.	33
Figure 3.6	The calculated electronic band structures of silicon allotropes III, M4, BCT, and IV.	34
Figure 4.1	A type II clathrate quantum dot and its meta-structure.	38
Figure 4.2	Meta-structures for several clathrate quantum dots composed of clathrates type I through VII and type H.	39
Figure 4.3	A series of type II silicon clathrate quantum dots composed of incomplete surface cages.	40
Figure 4.4	HOMO/LUMO gap as a function of unrelaxed quantum dot size for diamond silicon, clathrates type I, II, III, IV, V, VI, VII, VIII, and H. . . .	41
Figure 4.5	Quantum confinement sensitivity for two exponential relationships to dot diameter.	42
Figure 5.1	Confinement sensitivity parameter, $A^{(EMA)}$, is plotted against the inverse of the bulk, reduced effective mass, m^*	48
Figure 6.1	Values of the confinement sensitivity for two different power laws, d^{-2} (gray) and $d^{-1.55}$ (colored).	51

LIST OF TABLES

Table 2.1	Constraints, parameters, and pseudopotentials used for this work by data set.	23
Table 3.1	Calculated Structural information.	27
Table 3.2	Structural information of diamond silicon and seven other silicon allotropes.	27
Table 3.3	The RPA dielectric constant for silicon clathrates type I, II, IV, V, VI, and diamond silicon.	27
Table 3.4	The six directions in reciprocal space used to calculate the effective mass.	29
Table 3.5	The reduced effective masses for diamond silicon, clathrate types I-VIII and type H.	30
Table 3.6	Calculated valence band effective masses and published valence band effective masses for well known materials.	31
Table 3.7	Calculated conduction band effective masses and published conduction band effective masses for well known materials.	31
Table 5.1	Confinement constants and reduced effective masses for diamond silicon, clathrate types I-VIII and type H.	48
Table A.1	Values of KGridCutOff for different materials.	59

LIST OF SYMBOLS

charge of an electron	e
mass of an electron	m_e
electron positions	r_i
ion positions	R_i
ion charge	Z
many body wavefunction	$\psi(r_1 r_2 \dots r_n)$
electron density	$n(r)$
single particle wavefunction	$\psi(r)$
identity	I
hamiltonian for either many particles or a single particle	\hat{H}
creation operator of state ψ	a_ψ^\dagger
annihilation operator of state ψ	a_ψ
occupation of state ψ	n_ψ or N_ψ
symmetry factor/eigenvalues of the transposition operator	γ
eigenvalue	λ

LIST OF ABBREVIATIONS

Multiple Exciton Generation	MEG
Effective Mass Approximation	EMA
Random Phase Approximation	RPA
Highest Occupied Molecular Orbital	HOMO
Valence Band Edge	VBE
Conduction Band Edge	CBE
Density Functional Theory	DFT
Born-Oppenheimer Approximation	BOA
Kohn-Sham	KS
Generalized Gradient Approximation	GGA
Perdew-Burke-Ernzerh	PBE
Spanish Initiative for Electronic Simulations with Thousands of Atoms	SIESTA
Ceperley-Alder	CA
Double Zeta Polarized	DZP

ACKNOWLEDGMENTS

I would like to acknowledge the GK-12 Learning Partnership and the Bechtel K-5 Education Excellence Initiative for the financial support. I would also like to thank the Colorado School of Mines Physics Department faculty, in particular Prof. James Bernard, Prof. David Wood and Prof. Mark Lusk. Finally, I would like to acknowledge my grandfather, Dr. Kurt Brawand, MD who passed away before the completion of this work. Thank you for making college possible for my father, my siblings and myself.

To my beautiful wife, a paper all about those little yellow bubbles.

CHAPTER 1

INTRODUCTION

This document serves three main purposes: (1) to introduce silicon clathrate quantum dots and their confinement characteristics; (2) to compare quantum confinement in these silicon clathrate quantum dots to five other phases of silicon; and (3) to suggest that these effects of quantum confinement can largely be predicted by a single bulk property, namely the reduced effective mass. It is the author's hope that this information will contribute to the discovery of new stable series of silicon quantum dots characterized by multiple exciton generation (MEG) and long exciton life times.

1.1 Background

Diamond silicon quantum dots (dSi QDs) are being considered for photovoltaic and light-emitting diode applications [1, 2, 3] because they have size-tunable optical properties and are composed of an element that is nontoxic and earth-abundant. Their rapid development has also benefited from decades of experience with silicon in both manufactured integrated circuit technology and photovoltaic cell production. It may be possible to further extend the technological reach of Si QDs, though, by considering other crystalline structures as well. For instance, quantum dots composed of alternative Si allotropes may exhibit higher absorption/emission cross sections, lower optical gaps or more easily engineered exciton relaxation pathways [4]. For example, control of the relative relaxation rates of the possible pathways can greatly enhance the power conversion efficiency of solar cells if the dominant relaxation channel is the generation of multiple electron-hole pairs or excitons from single photons—i.e. multiple exciton generation (MEG) [1, 2]. However, to effectively combine efficient MEG with solar concentration, it is necessary that the optical gap be lower than the bulk Si-I (dSi) value of 1.11 eV [5], but quantum confinement increases the effective gap

over that of the bulk semiconductor. Other semiconducting phases of Si may offer lower gaps that could address this issue.

1.1.1 High Pressure Phases

One approach is to consider silicon phases that form under high pressure. The subsequent removal of pressure can result in allotropes with small band gaps that can persist at ambient conditions. The most common of these, known as Si-III, is a slightly distorted tetrahedral structure [6, 7] and is preceded by the more distorted rhombohedral Si-XII phase upon release of pressure below ca. 8 GPa. Si-III is stable at room temperature, as verified both experimentally and computationally [8, 4]. Significantly, the band gap of bulk Si-XII has been experimentally measured to be 0.24 eV, and Si-III is a semi-metal in bulk [4]. Both phases are ideally suited for MEG if they can be created as quantum dots. Another, as yet only theoretically predicted, allotrope with a low band gap is the M4 phase [9]. However, Alivisatos and co-workers [10] studied the high pressure behavior of Si QDs (10-50 nm diameter) coated with 1.5 nm SiO₂ starting with Si-I QDs and did not observe the formation of Si-XII and Si-III phases. Instead the samples transformed into amorphous silicon (aSi) upon release of pressure. Similar results were obtained in experiments on alkane-terminated dots where only aSi remained after pressure release [11]. It may still be possible, though, to create stable high-pressure allotropes by creating them within an encapsulating matrix. For instance, one experiment on Si nanowires with a ca. 17 nm thick SiO₂ shell layer exhibited the formation of encapsulated Si-XII dots [12]. Likewise, Si-III was reported to be formed in alternating thin layers of Si (2-5 nm) and SiO₂ (3 nm) [13].

1.1.2 Clathrates

While Si QDs composed of high pressure allotropes are just beginning to receive attention, and have encountered some technological obstacles to their synthesis, there is an entirely different class of Si crystals that have not been considered at all. Silicon can also be synthesized into a variety of periodic arrangements of covalently bonded cages. These

are typically formed when Si surrounds a reactive precursor, e.g. sodium, so as to make an encapsulating framework of distorted Si SP³ bonds. Initial encapsulations then serve as a template for further growth with the emerging crystal structure dependent on both thermodynamic state as well as kinetic considerations [14]. Perhaps surprisingly, these *silicon clathrates* have hydrate analogs that are common in nature [15] that can be found in vast quantities in oceanic sediments along the continental margins and in sediments under the permafrost in arctic regions. There hydrogen bonding of water molecules is the counterpart to the covalently bonded Si. However, the guest molecule around which the hydrates form is required to maintain stability, while silicon are stable without guest species, which can be subsequently removed by chemical or physical methods [16].

Silicon clathrate materials, which can be synthesized with a variety of dopants and/or guest species, have a broad spectrum of potential renewable energy applications, including thermoelectrics [17, 18], superconductors [19, 20], and photovoltaics [21, 22, 23]. However, only two crystalline structures of silicon clathrate have been synthesized to date: the type I structure composed of Si-24 and Si-20 cages; and the type II structure composed of Si-28 and Si-20 cages [24]. Of the two, only type II has been prepared guest-free, with an optical gap of 1.9 eV [25]. A wide range of other Si clathrate crystals have been theoretically proposed [26], however, and these are predicted to have a range of optical gaps that extend both above and below that of diamond Si.

The notion of clathrate Si quantum dots has not yet been considered, but it may well be that such structures offer optoelectronic properties comparable to those of dots composed of the semi-conducting high-pressure allotropes. These should be stable under ambient conditions and may be relatively easy to synthesize. As a first step towards exploring their promise, we have carried out a computational analysis of the confinement properties of dots composed of nine different clathrate crystal structures: Types I-VIII as well as Type H. Bulk crystal structures were also examined computationally in order to derive a means of predicting the sensitivity to confinement based on bulk character. The same analysis was

also carried out on diamond silicon and the high pressure allotropes Si-III, Si-XII and Si-M4 in order to provide a quantitative comparison.

CHAPTER 2

COMPUTATIONAL METHODS

“A computer lets you make more mistakes faster than any other invention, with the possible exceptions of handguns and Tequilla.”—Mitch Ratcliffe

All the results in this work were obtained through the labor of “great calculating machines”. It is therefore important to explain the methods and parameters used to generate these results. In this section I will leave the *historia salutis* of density functional theory to the authors of several other volumes. Instead, I would like to begin with the time independent Schrodinger equation and, in a heuristic manner, expose the clear difficulties associated with solving the quantum many body problem. After this the reader should understand the need to solve the problem through alternate methods. I will then present all the required theorems and approximations needed to make density functional theory a viable solution to our quantum many body problem. Within this step I will take a lengthy detour of the exchange and correlation energy of the jellium model because the thought of dry toast for breakfast could fetter even the most cheerful spirit to an anchor of melancholy and also, to motivate the local density approximation. After this lengthy detour of density functional theory I will summarize the role of density functional theory in the tasks performed and outline the specific implementations and parameters used to obtain the results reported in this paper.

2.1 Density Functional Theory

This section contains the motivation for and a quick outline of density functional theory.

2.1.1 Motivation: Riding The Wave Function

Imagine we have a crystal composed of electrons and nuclei. A proton or a neutron in this system is 1800 times more massive than that of the electrons outside of each nuclei. As these massive nuclei move in the crystal, the electrons surrounding them should move much more rapidly. This is an important point because it allows us to separate our problem into two pieces, one for electrons and one for the nuclei. This mathematical separation is called the Born-Oppenheimer approximation (BOA). The crystal Hamiltonian (with the BOA) can be written as,

$$\hat{H} = \underbrace{-\frac{\hbar^2}{2m_e} \sum_i \nabla_i^2 + \frac{e^2}{2} \sum_{i,j} \frac{1}{|r_i - r_j|}}_{H_{electron}} \underbrace{-\frac{\hbar^2}{2M} \sum_I \nabla_I^2 + \frac{e^2}{2} \sum_{I,J} \frac{1}{|R_I - R_J|}}_{H_{ion}} \underbrace{-\frac{1}{2} \sum_{i,J} \frac{e_i Z_J}{|R_i - R_J|}}_{H_{electron-ion}} \quad (2.1)$$

The time independent Schrodinger equation for the electron and electron-ion pieces can be written as,

$$\left(-\frac{\hbar^2}{2m_e} \sum_i \nabla_i^2 + \frac{e^2}{2} \sum_{i,j} \frac{1}{|r_i - r_j|} - \frac{1}{2} \sum_{i,J} \frac{e_i Z_J}{|r_i - R_J|} \right) \psi(r_1 r_2 \dots r_n) = E \psi(r_1 r_2 \dots r_n) \quad (2.2)$$

where R and J correspond to the coordinates and the sum over the nuclei. Like with most problems in physics we assume the wave functions to be a product of individual particle wave functions. This is known as the Hartree product or independent particle approximation.

Thus we write the wave function as,

$$\psi(r_1 r_2 \dots r_n) = \psi_1(r) \psi_2(r) \psi_3(r) \dots \psi_N(r) \quad (2.3)$$

Because of the spin statistics theorem we must remember that for our electrons that the wave function must be anti-symmetric so we would have to apply the anti-symmetrizer as mentioned in Section 2.2 but we will ignore this for the time being. Imagine now that you have a single lead atom (Pb). This atom has 82 electrons. Ignoring the nuclei, equation 2.2 is now requires 246 dimensions. If you were to consider a single cell of lead you would

have 984 dimensions on your hands. Hopefully these numbers are discouraging you from using 2.2 as it stands for any complex many body problem. It is worth noting that the wave function for any particular set of coordinates cannot be directly observed anyways. What is measured is the probability that the electrons are at a particular location. So one might suggest, why not abandon the independent particle wave function and reformulate the problem using the probability density? That sounds like a fantastic idea and is the focus of the following section.

2.1.2 It's All About the Density

The full crystal Hamiltonian is impossible to solve exactly. Furthermore, under the independent particle approximation, each anti-symmetrized multi-particle electron wave function contains $3n$ coordinates, where n is the number of electrons. Rather than work with such states it would be extremely nice if we could express the energy of the system in terms of a functional of the electron density. Lucky for us two theorems by Hohenberg and Kohn suggest just that. The theorems can be stated as follows,

- Theorem 1: The external potential of a system of interacting particles uniquely defines, up to a constant, the ground state particle density. *Therefore all properties of the system are defined by the ground state electron density.*
- Theorem 2: For any system, the energy functional $E[n(r)]$ can be defined. The density $n(r)$ that minimizes the energy is the exact ground state density for that system.

These wonderful results have now reduced our $3n$ dimensional problem to a 3 dimensional problem and tells us exactly what too look for, namely the electron density that minimizes the energy of the system.

With these in hand we set out to express our crystal Hamiltonian as a functional of the electron density. Let us begin by building up the needed components to do this starting with the electron density.

The electron density can be constructed from the sums of the squares of the orbitals for each spin,

$$n(r) = \sum_{\sigma,i} |\psi_{\sigma,i}(r)|^2 \quad (2.4)$$

The independent-particle kinetic energy is given by,

$$K = -\frac{1}{2} \sum_{\sigma,i} \langle \psi_{\sigma,i}(r) | \nabla^2 | \psi_{\sigma,i}(r) \rangle \quad (2.5)$$

For the coulomb interaction between electrons we can imagine just using a classical expression,

$$U_{Hartree} = \frac{e^2}{2} \int d^3r d^3r' \frac{n(r)n(r')}{|r-r'|} \quad (2.6)$$

The electron-ion interaction is given by,

$$U_{e-i} = \frac{1}{2} \int d^3r V(r)n(r) \quad (2.7)$$

where $V(r)$ is the external potential created by the ions in the lattice. We must also include the exchange and correlation terms as previously mentioned in Section 2.2.2. We will revisit these in a moment but for now we will write their contribution as $E_{xc}[n(r)]$. Thus the electronic portion of our system looks like,

$$\begin{aligned} E_{electron}[n(r)] = & -\frac{1}{2} \sum_{\sigma,i} \langle \psi_{\sigma,i}(r) | \nabla^2 | \psi_{\sigma,i}(r) \rangle + \frac{e^2}{2} \int d^3r d^3r' \frac{n(r)n(r')}{|r-r'|} \dots \\ & \dots + \frac{1}{2} \int d^3r V(r)n(r) + E_{xc}[n(r)] \quad (2.8) \end{aligned}$$

So far we have reduced a 3n problem to a 3 dimensional problem but how do we solve for $n(r)$? Is this really any easier than the TISE? These questions were answered when Kohn and Sham showed that the ground state electron density can be constructed from wave functions that belong to single electron equations! These series of single electron equations can be written as,

$$\left(-\frac{\hbar^2}{2m_e} \nabla_i^2 + V_{e-e}[r, n(r')] - +V_{e-i}(r) + V_{xc}[n(r)] \right) \psi_i(r) = E_i \psi_i(r) \quad (2.9)$$

where

$$V_{e-e}[n(r)] = \frac{\delta U_{Hartree}[n(r')]}{\delta n(r)} \quad (2.10)$$

$$= \frac{e^2}{2} \frac{\delta}{\delta n(r)} \int d^3r' d^3r'' \frac{n(r')n(r'')}{|r' - r''|} \quad (2.11)$$

$$= \frac{e^2}{2} \left(\int d^3r' d^3r'' \frac{n(r'')}{|r' - r''|} \delta(r - r') + \int d^3r' d^3r'' \frac{n(r')}{|r' - r''|} \delta(r - r'') \right) \quad (2.12)$$

$$= \frac{e^2}{2} \left(\int d^3r'' \frac{n(r'')}{|r - r''|} + \int d^3r' \frac{n(r')}{|r' - r|} \right) \quad (2.13)$$

$$= \boxed{e^2 \int d^3r' \frac{n(r')}{|r - r'|}} \quad (2.14)$$

is called the Hartree potential. The V 's in 2.9 are potentials. They are defined by the functional derivatives with respect to the density of the energy terms in 2.8. For example, the functional derivative with respect to the density of $E_{e-e} = \frac{e^2}{2} \int d^3r d^3r' \frac{n(r)n(r')}{|r-r'|}$ in 2.8 is $\frac{\delta E_{e-e}[n(r)]}{\delta n(r)} = V_{e-e}[n(r)]$ defined above.

The difference between 2.9 and 2.2 is now we can express our Hamiltonian as a function of electron density AND we only have to deal with 1 electron at a time! But wait, an unphysical monstrosity lurks within the Hartree potential. A careful reader might notice that IF $n(r')$ (in the Hartree potential) includes the contribution of the electron in state ψ_i , then there will be some part of the integral in the Hartree potential where the single electron is interacting with itself. Oh the horrors! How could one account for this single electron self interaction? As physicist do so often, we exhibit a supine acceptance of this corruption in V_{e-e} and sweep its correction into the term V_{xc} .

It is also worth pointing out that the Hohenberg and Kohn theorems only speak of the electron density and the total energy. The theorems do not mention anything about the Kohn-Sham orbitals ψ_i and eigen values E_i . These values belong to the auxiliary system and there is no guarantee that even for a converged calculation that they correspond to

reality. It was not till after the 1980's, or so I am told, that people started taking ψ_i and E_i seriously. That being said, keep in mind that as you look at all the band structure calculations and orbital energies in this document that you are looking at the solutions to equation 2.9.

As I have promised a couple times previously we will talk more about this mystery functional in 2.2 but for now lets discuss how we can use all this machinery.

2.1.3 Putting It All Together

Now that we have all the ingredients out on the table, let us bake this cake. The goal is to calculate $E_{tot-electron}$ from 2.8. Here is the recipe:

1. Guess an initial electron density $n(r)$ from equation 2.4 for your system.
2. Use that $n(r)$ to construct the potentials in Kohn-Sham equations (equation 2.9). Then solve for ψ_i .
3. With the new ψ_i 's construct a new $n(r)$ using equation 2.4.
4. Compare this new $n(r)$ from step 3 with the original $n(r)$ used in the Kohn-Sham equations in step 2.
5. If the two $n(r)$'s are the same (or close enough to the same), use that $n(r)$ to calculate $E_{tot-electron}$ using 2.8. If the two $n(r)$'s are different then use the new $n(r)$ to construct the potentials in the Kohn-Sham equations and repeat steps 2 through 5.

The only part we do not have is the exchange-correlation functional. This mystery term comes from all the cumbersome symmetrization constraints on the multiparticle wave functions. In general the true form of the exchange-correlation functional is not known but fortunately the exchange term can be derived exactly for one simple system. This system is the called the jellium model. In the jellium model we can calculate the exchange-correlation potential as a function of electron density. We then use this jellium exchange-correlation

potential as an approximation for our system by using it in the Kohn-Sham equations. We derive the jellium exchange energy per particle in the next section. Now that you have your cake, let us talk about jelly.

2.2 The Exchange and Correlation Energy of Jelly

In this section I derive the exchange energy per particle in the jellium model.

2.2.1 Background Information

Before we begin our voyage into a sea of indices, let us start with something familiar. The time independent Schrodinger equation, written simply as,

$$\hat{H}|\psi\rangle = E|\psi\rangle \quad (2.15)$$

Consider now we would like to describe a system that consists of many particles. We now need to define a space for each individual particle that we would like to describe. We do this by defining a state space for N particles.

$$\hat{H}_N = \dots I \otimes I \otimes \hat{H}_1 \otimes I \otimes I \dots + \dots I \otimes I \otimes \hat{H}_2 \otimes I \otimes I \dots + \dots I \otimes I \otimes \hat{H}_N \otimes I \otimes I \dots \quad (2.16)$$

$$= \hat{H}_1 \otimes \hat{H}_2 \otimes \hat{H}_3 \otimes \dots \otimes \hat{H}_N \quad (2.17)$$

$$= \prod_{n=1}^N \hat{H}_n \quad (2.18)$$

where \otimes is the tensor product. Above \hat{H}_i is the Hilbert space of the i-th particle. OK now that we have a tensor products of Hilbert spaces, we now need some fancy new state vectors to go along with it. For this we let $\{\psi_i\}$ be a complete set of commuting observables for the i-th Hilbert space of the i-th particle. A basis for our N particle system then consists of all possible tensor products of the one particle basis states,

$$|\Psi_N\rangle = |\psi_1\rangle \otimes |\psi_2\rangle \otimes |\psi_3\rangle \dots \otimes |\psi_N\rangle \quad (2.19)$$

where $|\psi_i\rangle$ is the orthonormal basis state for the i-th particle. Now say we would like to calculate $E_N = \langle \Psi_N | \hat{H}_N | \Psi_N \rangle$.

$$E_N = \langle \Psi_N | \hat{H}_N | \Psi_N \rangle \quad (2.20)$$

$$= \langle \Psi_N | \hat{H}_1 \otimes \hat{H}_2 \otimes \dots \otimes \hat{H}_N | \Psi_N \rangle \quad (2.21)$$

$$= \langle \Psi_N | \hat{H}_1 \otimes \hat{H}_2 \dots \otimes \hat{H}_N | \Psi_N \rangle \quad (2.22)$$

$$= \langle \psi_1 | \otimes \langle \psi_2 | \dots \otimes \langle \psi_N | \hat{H}_1 \otimes \hat{H}_2 \dots \otimes \hat{H}_N | \psi_1 \rangle \otimes | \psi_2 \rangle \dots \otimes | \psi_N \rangle \quad (2.23)$$

$$= \langle \psi_1 | \otimes \langle \psi_2 | \dots \otimes \langle \psi_N | \dots I \otimes I \otimes \hat{H}_1 \otimes I \otimes I \dots + \dots I \otimes I \otimes \hat{H}_2 \otimes I \otimes I \dots \quad (2.24)$$

$$\dots + \dots I \otimes I \otimes \hat{H}_N \otimes I \otimes I \dots | \psi_1 \rangle \otimes | \psi_2 \rangle \dots \otimes | \psi_N \rangle \quad (2.25)$$

$$= \langle \psi_1 | \hat{H}_1 | \psi_1 \rangle + \langle \psi_2 | \hat{H}_2 | \psi_2 \rangle \dots + \langle \psi_N | \hat{H}_N | \psi_N \rangle \quad (2.26)$$

$$= \epsilon_1 \langle \psi_1 | \psi_1 \rangle + \epsilon_2 \langle \psi_2 | \psi_2 \rangle \dots + \epsilon_n \langle \psi_N | \psi_N \rangle \quad (2.27)$$

$$= \epsilon_1 + \epsilon_2 \dots + \epsilon_N \quad (2.28)$$

As expected, the energy of an system with N particles is the sum of all the individual particle energies.

Now because the particles are indistinguishable, despite the fact that we label them as the “i-th particle”, a measurement of any observable should remain invariant under arbitrary applications of the permutation operator. What I mean is this,

$$\langle a_1 b_2 | \hat{O} | a_1 b_2 \rangle = \langle a_2 b_1 | \hat{O} | a_2 b_1 \rangle \quad (2.29)$$

Here we have taken particle 1 which was in state a and placed it in state b and did the opposite for particle 2. This has interesting consequences and as we already know wave functions that satisfy these conditions belong to two categories.

1. Symmetric wave functions - bosons
2. Anti-symmetric wave functions - fermions

To proceed with these symmetry constraints on our wave functions we have two options. First we could continue down the road we are on with something called the symmeterizer, this dreadful thing is cumbersome, or we can wrap up all of the symmetry constraints into the commutation relations of creation and annihilation operators. I suggest we go the route of commutation relations.

2.2.1.1 The State of the Vacuum

As I mentioned before, working with the symmeterizer can really be painful. Instead, let us work with creation and annihilation operators. To do this we need to define a special state, the vacuum state! This state is best introduced in the form of a story. While I am at it I will introduce the creation and annihilation operators. Here is how the story goes, In the beginning was

$$|0\rangle \tag{2.30}$$

and the physicist said,

$$a_\psi^\dagger |0\rangle \tag{2.31}$$

and there was

$$\sqrt{0+1}|\psi\rangle \tag{2.32}$$

The physicist, also by fiat command, created all sorts of other crazy things,

$$a_\xi^\dagger a_\beta^\dagger a_\alpha^\dagger |\psi\rangle = a_\xi^\dagger a_\beta^\dagger \sqrt{1+1}|\alpha\psi\rangle \tag{2.33}$$

$$= a_\xi^\dagger \sqrt{2}\sqrt{2+1}|\beta\alpha\psi\rangle \tag{2.34}$$

$$= \sqrt{2}\sqrt{2+1}\sqrt{3+1}|\xi\beta\alpha\psi\rangle \tag{2.35}$$

$$= 2\sqrt{6}|\xi\beta\alpha\psi\rangle \tag{2.36}$$

And the physicist saw that $2\sqrt{6}|\xi\beta\alpha\psi\rangle$ was kinda good but really wished he hadn't made α so he sent the hermitian conjugate of a_α^\dagger to annihilate α .

$$a_\alpha 2\sqrt{6}|\xi\beta\alpha\psi\rangle = \frac{2\sqrt{6}}{\sqrt{4}} (\gamma^0 \langle \alpha | \xi \rangle |\beta\alpha\psi\rangle + \gamma^1 \langle \alpha | \beta \rangle |\xi\alpha\psi\rangle + \gamma^2 \langle \alpha | \alpha \rangle |\xi\beta\psi\rangle + \gamma^3 \langle \alpha | \psi \rangle |\xi\beta\alpha\rangle) \tag{2.37}$$

$$= \sqrt{6}\gamma^2 |\xi\beta\psi\rangle \tag{2.38}$$

I have not mentioned what γ was yet but γ is 1 for bosons and -1 for fermions. So in this case of either fermions or bosons we would have obtained $\sqrt{6}|\xi\beta\psi\rangle$. If we had annihilated β

from the original state we would have obtained one factor of γ and that would have given us a factor of -1 for fermions. Now that we understand how the creation and annihilation operators work we can move to their commutation relations.

2.2.1.2 Some Operators Carpool, Some Do Not

It is important to know how to derive these commutation relations, but at the end of the day the most important thing is that you just memorize them so you can use them. Remember that γ is 1 for bosons and -1 for fermions. Here they are,

$$[a, b]_\gamma = ab - \gamma ba \quad (2.39)$$

$$[ab, c]_\gamma = a[b, c]_\gamma + [a, c]_\gamma b \quad (2.40)$$

$$[a_\alpha, a_\beta]_\gamma = 0 \quad (2.41)$$

$$[a_\alpha^\dagger, a_\beta^\dagger]_\gamma = 0 \quad (2.42)$$

$$[a_\alpha, a_\beta^\dagger]_\gamma = \langle \alpha | \beta \rangle \quad (2.43)$$

$$n_\alpha = a_\alpha^\dagger a_\alpha \quad (2.44)$$

$$N = \sum_\alpha n_\alpha \quad (2.45)$$

2.2.1.3 Operators of Operators

Now that we have all the basic components we can construct other operators from the number operator n . For example say we wanted the total kinetic energy of a system with four particles. Two of these particles are in state α , 1 in state β and another in state ξ with kinetic energy eigen values of λ_α , λ_β , and λ_ξ respectively. The total kinetic energy would be,

$$T_{N=4} = 2\lambda_\alpha + 1\lambda_\beta + 1\lambda_\xi \quad (2.46)$$

If we wanted to obtain this result by acting on a multi-particle state in the orthonormal basis it would be plausible to write,

$$\langle 2_\alpha 1_\beta 1_\xi | T_N | 2_\alpha 1_\beta 1_\xi \rangle = \langle 2_\alpha 1_\beta 1_\xi | \sum_i \lambda_i a_i^\dagger a_i | 2_\alpha 1_\beta 1_\xi \rangle = \langle 2_\alpha 1_\beta 1_\xi | \sum_i \lambda_i n_i | 2_\alpha 1_\beta 1_\xi \rangle \quad (2.47)$$

where the number in the state vector represents the number of particles in that state. For example 2_α means there are two particles in state α . In general we can write any one body operator as,

$$\hat{O} = \sum_{i,j} \lambda_{i,j} a_i^\dagger a_j \quad (2.48)$$

A two body operator, like the coulomb interaction, can be written as,

$$\hat{U} = \sum_{i,j,k,l} \langle n_i n_j | T_N | n_k n_l \rangle a_i^\dagger a_j^\dagger a_l a_k \quad (2.49)$$

Notice the flipped order of the two annihilation operators. This only matters when one is dealing with fermions.

2.2.2 A Positive Background

We now apply all the machinery developed in the previous section to the Jellium model. The model in this case is a sea of electrons running around in a constant positively charged background. I suppose if you imagined grinding up all the positively charged ion cores in a solid you would get this positively charged background that you could smear out like jelly... It must have been breakfast time when this idea was conceived. Anyways, let us take our crystal of volume V with N total electrons and make jelly out of our ions. Now we have a uniform background density of N/V . Our Hamiltonian is,

$$H_{model} = H_{electron} + H_{jelly} + H_{ej} \quad (2.50)$$

where H_{jelly} is the energy of our positively charged background and H_{ej} is the energy of the interaction between the electrons and the jelly. Here we want to uncover the exchange and correlation energy. Therefore we are interested in $H_{electron}$. Using perturbation theory we define,

$$H_{electron} = H_T + H_{ee} = H + H' \quad (2.51)$$

where H_T is the kinetic energies of the electrons and H_{ee} , our perturbation is the electron-electron interaction. If one were to write down H' in terms of plane waves and used the Yukawa potential, eventually they could work H' into the following expression,

$$H' = \frac{1}{2} \sum_{k1, k2, q \neq 0} U_q a_{k1+q}^\dagger a_{k2-q}^\dagger a_{k2} a_{k1} \quad (2.52)$$

where $U_q(\alpha) = \frac{4\pi e^2}{Vq^2}$. If your wondering, α came from the decay constant of the Yukawa potential. Also, q can be interpreted as the momentum exchange between $k1$ and $k2$. From perturbation theory the first order correction of the energy is,

$$E_0^{(1)} = \langle E_0 | H' | E_0 \rangle \quad (2.53)$$

$$= \frac{2\pi e^2}{V} \langle E_0 | \sum_{k1, k2, q \neq 0} \frac{1}{q^2} a_{k1+q}^\dagger a_{k2-q}^\dagger a_{k2} a_{k1} | E_0 \rangle \quad (2.54)$$

$$= \frac{2\pi e^2}{V} \sum_{q \neq 0} \sum_{k1, k2} \frac{1}{q^2} \langle E_0 | a_{k1+q}^\dagger a_{k2-q}^\dagger a_{k2} a_{k1} | E_0 \rangle \quad (2.55)$$

There are two options that yield non-zero results.

1. a_{k1} takes electron one from state $|k1\rangle$ and puts it in $|k1 + q\rangle$. Meanwhile a_{k2} takes electron two from state $|k2\rangle$ and puts it in state $|k2 - q\rangle$. This is called the *direct* process.
2. a_{k1} takes electron one from state $|k1\rangle$ and puts it in $|k2 - q\rangle$. Meanwhile a_{k2} takes electron two from state $|k2\rangle$ and puts it in state $|k1 + q\rangle$. This is called the *exchange* process.

Thus the exchange process is the “swapping of particle labels”. By using the commutation relations outlined previously one can show that,

$$E_0^{(1)} = -\frac{4\pi e^2}{2V} \sum_{q \neq 0} \sum_k \frac{1}{q^2} \langle E_0 | N_{k+q} N_k | E_0 \rangle \quad (2.56)$$

The matrix element vanishes unless both states $k + q$ and k are occupied in the ground state $|E_0\rangle$. Thus $\langle E_0 | N_{k+q} N_k | E_0 \rangle = \Theta(k_f - |k + q|) \Theta(k_f - |k|)$. Converting our sums to integrals we can write the first order energy shift as,

$$E_0^{(1)} = -\frac{4\pi e^2 V}{(2\pi)^6} \int d^3 q \frac{1}{q^2} \int d^3 k \Theta(k_f - |k + q|) \Theta(k_f - |k|) \quad (2.57)$$

Performing this integral one finally obtains $E_0^{(1)} = -\frac{e^2 V}{4\pi^3} k_f^4$. Expressing this in terms of the mean energy per particle and the bohr radius gives,

$$\frac{E_0^{(1)}}{N} = -\frac{3}{2\pi} k_f a_o \times 1Ry \quad (2.58)$$

The mean ground-state energy per electron in the jellium model is,

$$\frac{E_0}{N} = \frac{E_0^{(0)}}{N} + \frac{E_0^{(1)}}{N} + \frac{E_0^{(2)}}{N} + \dots = \frac{3}{5} (k_f a_o)^2 - \underbrace{\frac{3}{2\pi} k_f a_o}_{E_{exchange}} + E_{correlation} \quad (2.59)$$

$E_0^{(1)}$ was the exchange energy all along. The third term in the expansion is the correlation energy. The exchange energy is negative because of the antisymmetry of the wave function. Because of the symmetry requirements, two electrons with parallel spin will be farther apart than expected, thus reducing the coulomb interaction and that is why the exchange energy is negative. Now that we have seen the exchange and correlation energy in the jellium model, we now return to its application to density functional theory.

2.3 The Exchange-Correlation Functional

This section contains a quick overview of the LDA and other commonly used exchange-correlation functionals.

2.3.1 LDA

In the previous section we showed that the exchange energy per particle can be derived exactly for a uniform electron gas. When we calculate the exchange-correlation energy for a particular point in space in the Kohn-Sham equations, and only consider the density at that one point, using the exchange and correlation potential from the jellium model we call this the *local density approximation (LDA)*. In other words,

$$E_{xc}[n(r)] = \int d^3 r n(r) \epsilon_{xc}[n(r)] \quad (2.60)$$

where ϵ_{xc} is the energy per particle at point r , derived in the previous section (at least the “x” part of the “xc”). Notice how E_{xc} is only an integral over r , this means that the energy only depends on the density at point r . Hence the term *local* density approximation. As you might remember from the Kohn-Sham equation this showed up as the exchange-correlation *potential*. The potential is just the functional derivative of the energy.

$$V_{xc}[n(r)] = \frac{\delta E_{xc}[n(r')]}{\delta n(r)} \quad (2.61)$$

$$= \frac{\delta}{\delta n(r)} \int d^3r' n(r') \epsilon_{xc}[n(r')] \quad (2.62)$$

$$= \int d^3r' \delta(r - r') \epsilon_{xc}[n(r')] + \int d^3r' n(r') \frac{\delta \epsilon_{xc}[n(r')]}{\delta n(r)} \delta(r - r') \quad (2.63)$$

$$= \epsilon_{xc}[n(r)] + n(r) \frac{\delta \epsilon_{xc}[n(r)]}{\delta n(r)} \quad (2.64)$$

Again ϵ_{xc} is the exchange-correlation energy per particle we partially derived in 2.2. If one were to break up the electron density in a conventional cell into extremely small pieces the density would vary slowly from one position to another. Thus we can make the approximation that the density is constant and validate the use of the LDA. For a quick discussion of the paradoxical nature of this beast, I point the reader to section 7.3 of [27]. The LDA has some well known problems. For example the the exchange-correlation energy of a polarized insulator is not a function of only the density of a particular point but a function of the polarization in the neighborhood of that point. It is also well known that LDA underestimates the band gap of many semiconductors.

2.3.2 Other Functionals

Because of the success of the LDA, other functionals of increasing complexity have been developed. Figure Figure 2.1 quickly summarizes these other functionals.

Figure Figure 2.1 is slightly misleading, in that it suggests that the functionals higher along the ladder are always more accurate. This is not the case but they do include more physical information. We already mentioned LDA in the previous section so we should start

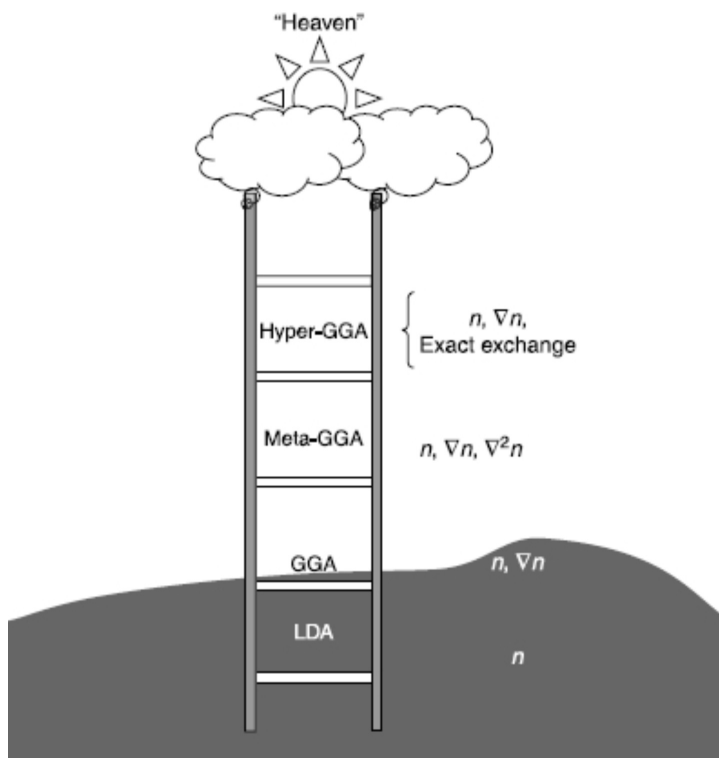


Figure 2.1: Jacob’s ladder of exchange-correlation functionals. Taken from [28].

with the generalized gradient approximation GGA. Because the electron densities in solids are not actually constant, we would expect that the exchange correlation energy should vary as the electron density does. Thus we expect the exchange-correlation potential to be a function of the density and its gradient.

$$V_{xc}^{GGA}[n(r), \nabla n(r)] \quad (2.65)$$

Two widely used non-empirical functionals that satisfy several known exact properties of the exchange-correlation hole are the Perdew-Wang 91 functional (PW91) and the Perdew-Burke-Ernzerh functional (PBE). Though GGA includes more information than LDA it is not always more accurate. Meta-GGA includes the Laplacian of the electron density. Like the Hartree-Fock method, hyper-GGA, the most commonly used in quantum chemistry calculations, includes the exact exchange energy. Unfortunately, functionals of this form are nonlocal causing them to be computationally expensive.

2.4 Geometry Optimization

So far we have shown that with DFT we are able to predict the ground state electron density and energy of a collection of atoms. But what if we wish to not only find the ground state electron density but also the ground state geometry of the atoms? By writing the total energy of the system as a function of atomic coordinates we can find the ground state geometry using DFT but to understand how it works I think we should take a quick detour of the conjugate gradient method.

2.4.1 The Conjugate Gradient Method

Like the more familiar (at least for me) Newton based methods the conjugate gradient method is a tool used to minimize a function with respect to its arguments. The conjugate gradient method can be summarized as follows. First make an initial estimate \mathbf{r}_0 of the minimum point of the function you wish to minimize, let us use $E[\mathbf{r}]$. The next point to guess the minimum, lies along the line,

$$\mathbf{r}_1 = -a\nabla E[\mathbf{r}_0] + \mathbf{r}_0 \quad (2.66)$$

where a is the step length. The optimal step length yields the next direction to be orthogonal to the original direction. In other words,

$$\nabla E[\mathbf{r}_i] \cdot \nabla E[\mathbf{r}_{i+1}] = 0 \quad (2.67)$$

where i is the i th step in the conjugate gradient method. To find the next direction we estimate the optimal step length and demand that the new direction be orthogonal to the original direction using,

$$-\nabla E[\mathbf{r}_{i+1}] = \frac{(\nabla E[\mathbf{r}_{i+1guess}] \cdot \nabla E[\mathbf{r}_i])}{\nabla E[\mathbf{r}_i] \cdot \nabla E[\mathbf{r}_i]} \nabla E[\mathbf{r}_i] - \nabla E[\mathbf{r}_{i+1guess}] \quad (2.68)$$

where $\nabla E[\mathbf{r}_{i+1guess}]$ is the estimate we obtained from 2.66 for the next search direction. Therefore you are removing any part of the next guess that happens to be parallel to the original direction. We then can use equation 2.66 again to obtain the next point and then we demand that the new search direction be orthogonal to all the previous search vectors.

Eventually we will run out dimensions to be orthogonal to so we will need to restart the process again. For an N dimensional system we will need to start the process after constructing a vector that is orthogonal to $N-1$ other vectors. If $E[\mathbf{r}]$ in this case is the energy of the system, then the expression $-\nabla E[\mathbf{r}]$ should look very familiar, it is the force. With this in view, we could interpret the conjugate gradient method as repeated steps along force vectors to reduce the energy of the system.

2.4.2 Relaxation in DFT

If we now think of the total energy as a function of all the atomic coordinates of the system and the electron density $E[\mathbf{r}_{1,2\dots N}, n(\mathbf{r})]$, we can use the conjugate gradient method to minimize the total energy of the system by moving the atoms along force vectors till they reach equilibrium. The steps are as follows,

1. Find the ground state energy of the system by solving the Kohn-Sham equations using the steps in section 2.1.3.
2. Using the conjugate gradient method, move each atom a small amount to minimize the the total energy of the system.
3. Repeat steps 1 and 2 till the maximum force tolerance is reached.

What force tolerance is reasonable? Well if we estimate the total change in the energy as $|\Delta E| = |F||\Delta r|$ where F is the maximum force, say 0.04 eV/ang, then moving any atom by .1 ang will result in a change of energy less than 0.004 eV. My argument is that 0.004 eV is a small amount of energy compared to the total energy of the system. Thus 0.04 eV/ang is a respectable force tolerance.

2.5 Methodology

The purpose of this section is to report the specific implementation of DFT that was used for this work. We will begin with a short overview of SIESTA[29] and then move to

the specific constraints and parameters used to generate the results reported in the sections below.

2.5.1 The Software Packages

SIESTA[29], the particular implementation of DFT used for this work, stands for Spanish Initiative for Electronic Simulations with Thousands of Atoms. SIESTA uses atomic orbitals as a basis for the Kohn-Sham wavefunctions and the standard Kohn-Sham self-consistent density functional method outlined in section 2.1.3 to perform efficient electronic structure calculations and ab initio molecular dynamics simulations of molecules and solids. Unlike all electron calculations, SIESTA uses norm-conserving pseudopotentials in their fully nonlocal (Kleinman-Bylander) form. Most of the results reported in this work were obtained from calculations performed by SIESTA but the ϵ_{RPA} 's reported in 3.2.2 were obtained using a software package called ABINIT[30].

2.5.2 Constraints and Parameters

All the results reported in this paper can be broken down into 2 categories, results belonging to bulk structures and results belonging to finite structures. These two categories each have two sub-categories belonging to two sets of data, one set of data is relaxed and the other set of data is un-relaxed. All the constraints, parameters, and pseudopotentials used for these four separate sets of data are summarized in table Table 2.1.

Table 2.1: Constraints, parameters, and pseudopotentials used for this work by data set.

Category	Bulk Structure		Finite Structure	
Sub-category	Relaxed	Un-relaxed	Relaxed	Un-relaxed
Software Package	SIESTA 3.1	SIESTA 3.1	SIESTA 3.0	SIESTA 3.1
MeshCutoff	>150 Ry	>150 Ry	>100 Ry	>150 Ry
KgridCutoff	See Appendix	See Appendix	n/a	n/a
PAO.BasisSize	DZP	DZP	DZP	DZP
DM.Tolerance	<0.0001	<0.0001	<0.0001	<0.0001
MD.MaxForceTol	<0.04 eV/Ang	n/a	<0.04 eV/Ang	n/a
ElectronicTemperature	0 meV	0 meV	0 meV	0 meV
XC.functional	LDA	LDA	LDA	LDA
XC.authors	CA	CA	CA	CA
Pseudopotentials	See Appendix	See Appendix	See Appendix	See Appendix

CHAPTER 3

PROPERTIES OF BULK CLATHRATES

As mentioned previously, clathrates are labeled using roman numerals. In this paper guest-free clathrate types I, II, III, IV, V, VI,VII, VIII, and H are studied. The purpose of this section is to introduce the geometry of these structures, their electronic band structures, dielectric constants, and their effective masses. Later these geometries will be used to construct a series of quantum dots and their effective masses will be show to correlate with quantum confinement of the HOMO/LUMO gap.

3.1 Structural Properties

Within this section, an overview of the geometries of the clathates is given. Following that, the calculated structural properties of both the clathate structures and other allotropes of silicon are reported.

3.1.1 Clathrates

Clathrates are networks composed of one or more face sharing polyhedra. For silicon clathrates, a single silicon atom resides at each vertex of the polyhedron and bonds are formed along the edges. To understand this, consider type VII clathrate found in Figure 3.1.

In terms of geometry, type VII clathrate is the simplest of all the clathrates studied here. It is composed of only one polyhedron, the truncated octahedron. A single truncated octahedron is made up of six rings with four atoms in each ring, and eight rings with six atoms in each ring. We denote the truncated octahedron as $[4^66^8]$.

Type VII clathrate only consisting of one polyhedron, which we will refer to as a “cage”. Other clathrates studied here are composed of two or more different cages. For a summary of the clathrate geometries considered here, refer to Figure 3.2.

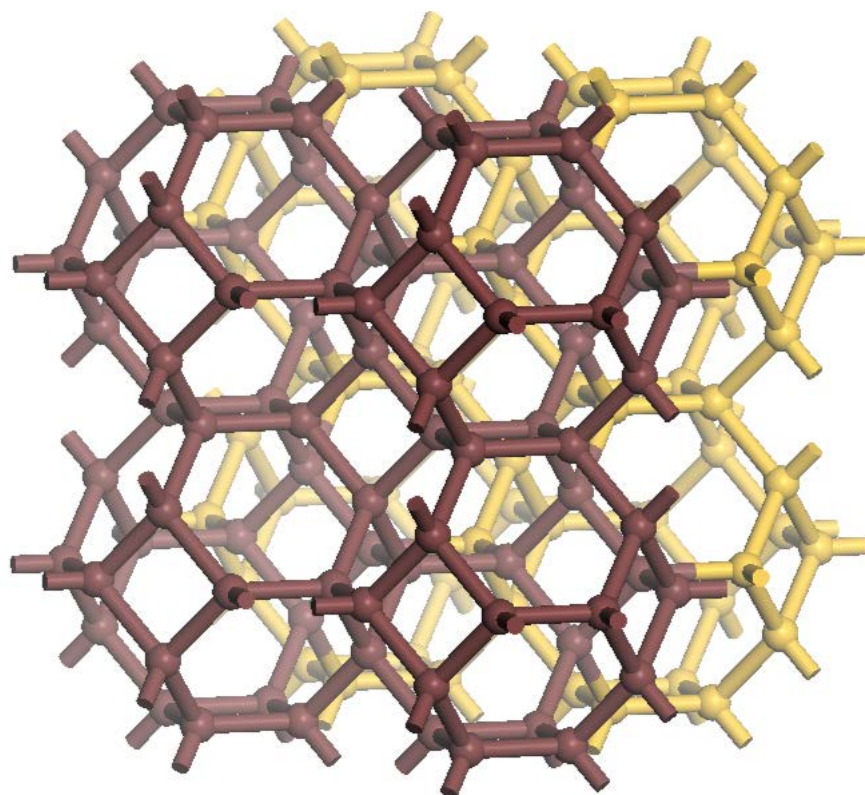


Figure 3.1: The geometry of type VII clathrate.

Each of the clathrates found in Figure 3.2 were relaxed using the methods and constraints mentioned in Chapter: 2. A summary of the results can be found in Table 3.1 and Figure 3.3.

3.1.2 Other Silicon Allotropes

Because the end goal of this research is to identify an allotrope of silicon that forms stable quantum dots with low optical gaps, it is important to compare the clathrate structures to other allotropes of silicon. The focus of this work is not on these particular structures so I will give a quick summary of their geometries in Table 3.2. Later the HOMO/LUMO gap of a series of quantum dots constructed from these bulk structures along with the clathrate structures will also be reported.

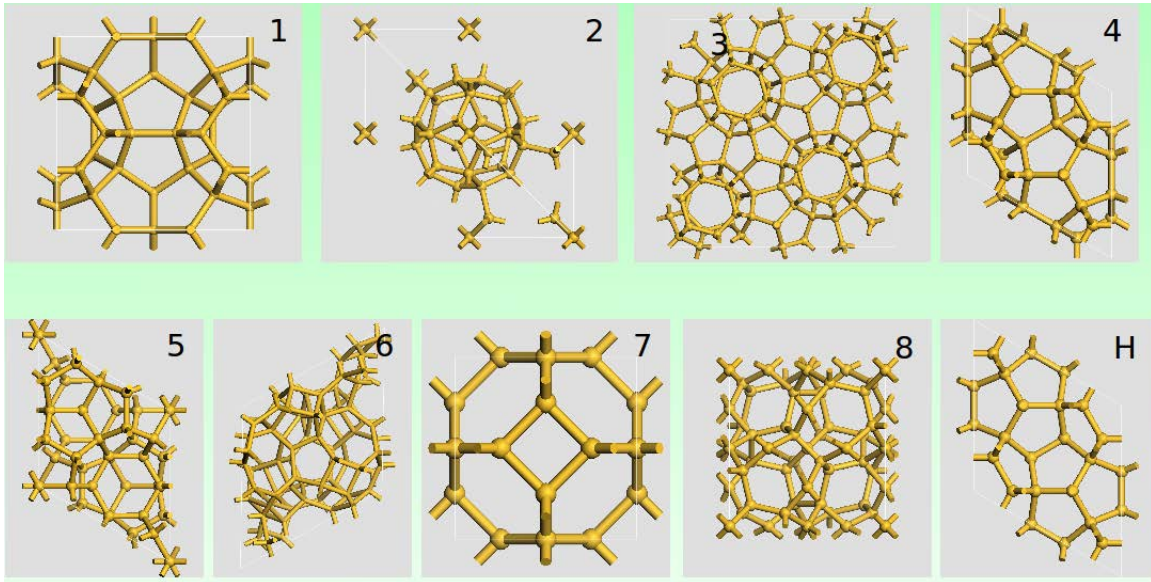


Figure 3.2: The geometry of clathrate structures I, II, III, IV, V, VI, VII, VIII, and H.

3.2 Electronic

Along with the structural relaxation, the electronic band structures were also calculated for both the clathrate structures and the other silicon allotropes mentioned in the previous section. These band structures are reported here.

3.2.1 Electronic Band Structures of The Silicon Clathrates

From the relaxed geometries given in 3.1.1 the electronic band structures were also calculated using the methods and constraints given in Chapter:2. These band structures are shown in Figure 3.4.

From the band structures in Figure 3.4, the edges of the valence and conduction bands were identified. The effective masses were then calculated from these positions in the brillouin zone. This information can be found in Section: 3.3.

3.2.2 Calculated Dielectric Constants for The Silicon Clathrates

Another important quantity that was calculated was the RPA dielectric constant. It was previously thought that a large portion of a materials confinement characteristics could be

Table 3.1: Calculated Structural information.

Clathrate	Primitive Cell Parameters (deg/ang)
I	90 90 90 10.36 10.36 10.36
II	90 90 90 14.58 14.58 14.58
III	90 90 90 19.37 19.37 11.23
IV	90 90 120 10.11 10.11 10.26
V	90 90 120 10.29 10.29 16.89
VI	90 90 90 15.77 15.77 15.77
VII	90 90 90 6.66 6.66 6.66
VIII	90 90 90 9.99 9.99 9.99
H	90 90 90 120 10.40 10.40 8.45

Table 3.2: Structural information of diamond silicon and seven other silicon allotropes.

Structure	Primitive Cell Parameters
DSi	60 60 60 3.84 3.84 3.84
Si III	109.47 109.47 109.47 5.75 5.75 5.75
Si XII	110.07 110.07 110.07 5.61 5.61 5.61
Si M4	90 90 90 13.90 3.86 6.36
Si IV	90 90 120 3.84 3.84 6.36
Si T12	90 90 90 5.14 5.14 9.17
Si BCT	90 90 90 6.686 6.686 3.859
Si Wurtzite	90 90 120 4.04 4.04 6.6

explained by screening. While this might be true due to the coulomb interaction between the electron and the hole, this interaction is not captured by a ground state DFT calculation where the exciton energy is approximated by the energy difference between the HOMO and the LUMO. Nevertheless, this quantity was calculated for clathrates type I, II, IV, V, VI, VII, VIII, and H using the methods and constraints mentioned before in 2. These values can be found in Table 3.3.

Table 3.3: The RPA dielectric constant for silicon clathrates type I, II, IV, V, VI, and diamond silicon.

Phase	DSi	I	II	IV	V	VI
ϵ_{RPA}	11	5	10	15	12	10

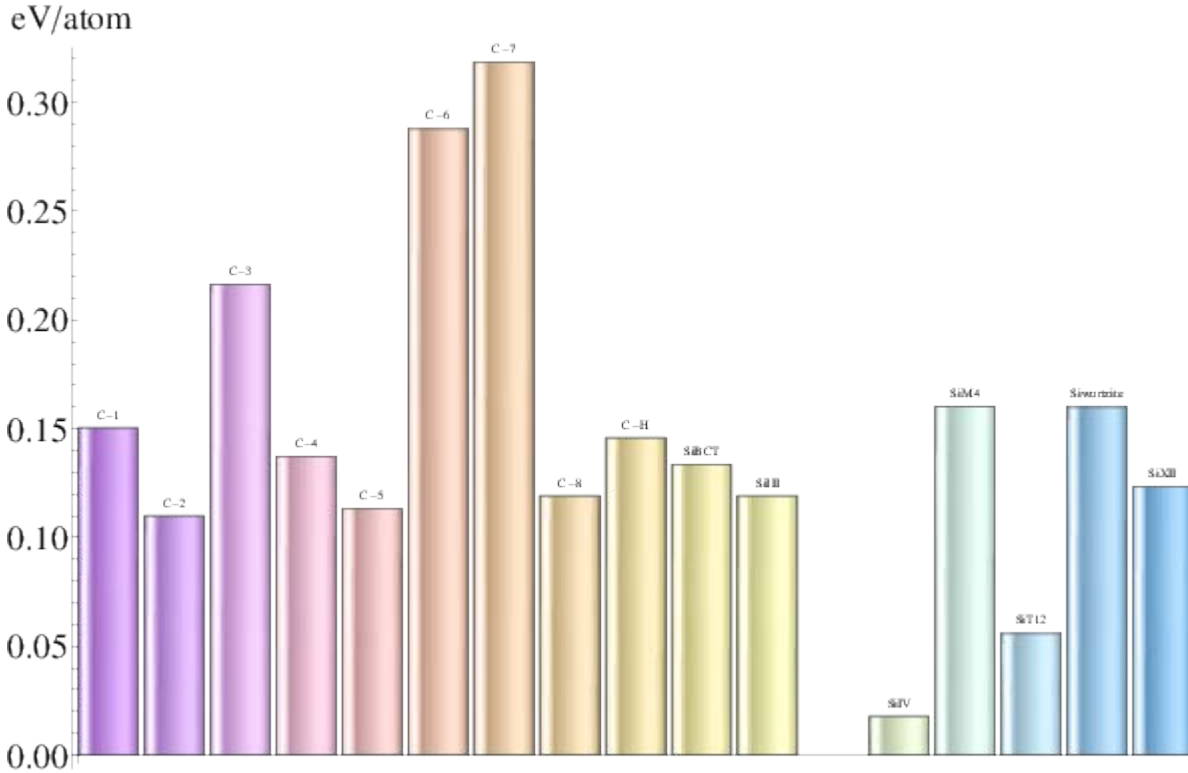


Figure 3.3: The energy per atom relative to diamond silicon for clathrates type I-VIII, H and seven other silicon allotropes. (L-R) clathrate types 1-8, H, non-clathrate Si allotropes BCT, III, diamond, IV, M4, T12, wurtzite, and XII.

3.2.3 Electronic Band Structures of The Other Silicon Allotropes

From the geometries given in 3.1.1 the electronic band structures were also calculated using the methods and constraints given in Chapter:2. These band structures are reported in Figure 3.5 and Figure 3.6.

3.3 Effective Masses

The final bulk quantity calculated was the reduced effective mass. As a material transitions from an infinite crystal to a finite structure, the wave vectors become discrete. For this work it is assumed that the shape of the band edges is parabolic and is maintained as the system becomes smaller. As this happens, the states at the band edges begin to separate and continue to move along the original parabola. Thus we expect the effective mass of a

bulk material to be an indicator of a material's sensitivity to quantum confinement.

In this section we will first explain how the effective mass was calculated. Next, the calculated values for clathrates type I-VIII and type H are reported and finally the accuracy of the method is evaluated by comparison with literature.

3.3.1 Methodology

The first step to calculate the effective mass is to locate the valence band edge (VBE) and the conduction band edge (CBE) in reciprocal space. This was done using the band diagrams mentioned in 3.2.1. Once located, if degeneracy exists at these points, then the band with the lightest effective mass was selected. This was done because it is thought that the confinement characteristics of the material would be dominated by the bands with the smaller effective masses.

Once the band index and wave vector was chosen, the Brillouin zone was sampled around these points in six directions for both the VBE and CBE separately. Resulting in twelve separate paths total. In Cartesian coordinates, the direction of the paths are found in Table 3.4.

Table 3.4: The six directions in reciprocal space used to calculate the effective mass.

direction number	1	2	3	4	5	6
vector in Cartesian coordinates	\hat{x}	\hat{y}	\hat{z}	$\frac{1}{\sqrt{2}}(\hat{x} + \hat{y})$	$\frac{1}{\sqrt{2}}(\hat{x} + \hat{z})$	$\frac{1}{\sqrt{2}}(\hat{y} + \hat{z})$

After these paths were calculated they were fitted to a parabola in mathematica. From these fitted parabolas the effective mass tensor is given by

$$m_{\mu,\nu}^* = \hbar^2 (\partial_{\mu,\nu} E(k))^{-1} \quad (3.1)$$

Where E is the energy as a function of wave vector k and $m_{\mu,\nu}^*$ is the effective mass tensor. The indices μ and ν correspond to the directions listed in Table 3.4.

Once obtained, the effective mass tensor was diagonalized and the elements were averaged in the following way to obtain the scalar effective mass m_s^* .

$$m_s^* = 3 \left(\delta^{\nu,\mu} (m^*)_{\mu,\nu}^{-1} \right)^{-1} \quad (3.2)$$

In this work we used the effective mass of conductivity to describe confinement as is also the case in [31].

After this, the reduced effective mass m^* was obtained by combining the scalar CBE effective mass m_e^* and scalar VBE effective mass m_h^* in the following way,

$$m^* = \frac{m_e^* |m_h^*|}{m_e^* + |m_h^*|} \quad (3.3)$$

This is the *reduced effective mass*.

3.3.2 Effective Mass Results

The effective masses for diamond silicon and clathrate types I-VIII and type H are displayed in Table: Table 3.5

Table 3.5: The reduced effective masses for diamond silicon, clathrate types I-VIII and type H.

Structure	dSi	Type I	Type II	Type III	Type IV
m^*	0 .13	0.29	0 .24	0.29	0.29
Structure	Type V	Type VI	Type VII	Type VIII	Type H
m^*	0 .35	0 .57	0 .15	0 .24	0 .20

3.3.3 Comparison With Literature

To give the reader a sense of the accuracy associated with these results, we have calculated values of m^* for various well known structures. This information is displayed in Table : Table 3.6 and Table 3.7.

Table 3.6: Calculated valence band effective masses and published valence band effective masses for well known materials.

Valence Band m^*	Published m^*	Calculated m^*	% Error	Absolute Error
dSi	0.36	0.26	27.50	0.1
dGe	0.21	0.22	5.71	0.01
dC	0.47	0.55	16.93	0.08
GaAs	0.34	0.28	17.94	0.06

Table 3.7: Calculated conduction band effective masses and published conduction band effective masses for well known materials.

Conduction Band m^*	Published m^*	Calculated m^*	% Error	Absolute Error
dSi	0.26	0.25	4.23	0.01
dC	0.36	0.40	12.29	0.04
GaAs	0.07	0.01	84.18	0.05

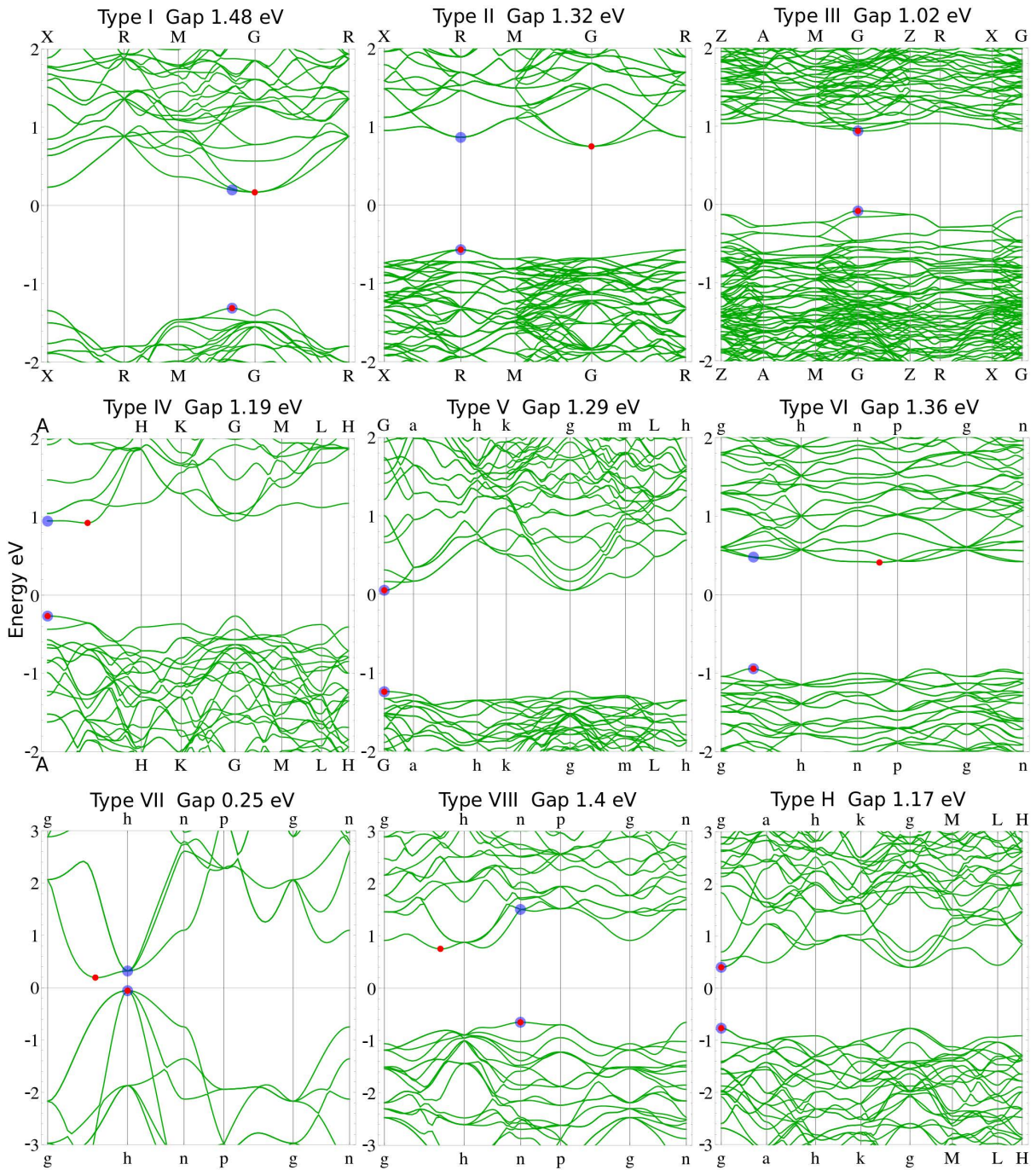


Figure 3.4: The calculated electronic band structures of silicon clathrates type I-VIII and type H.

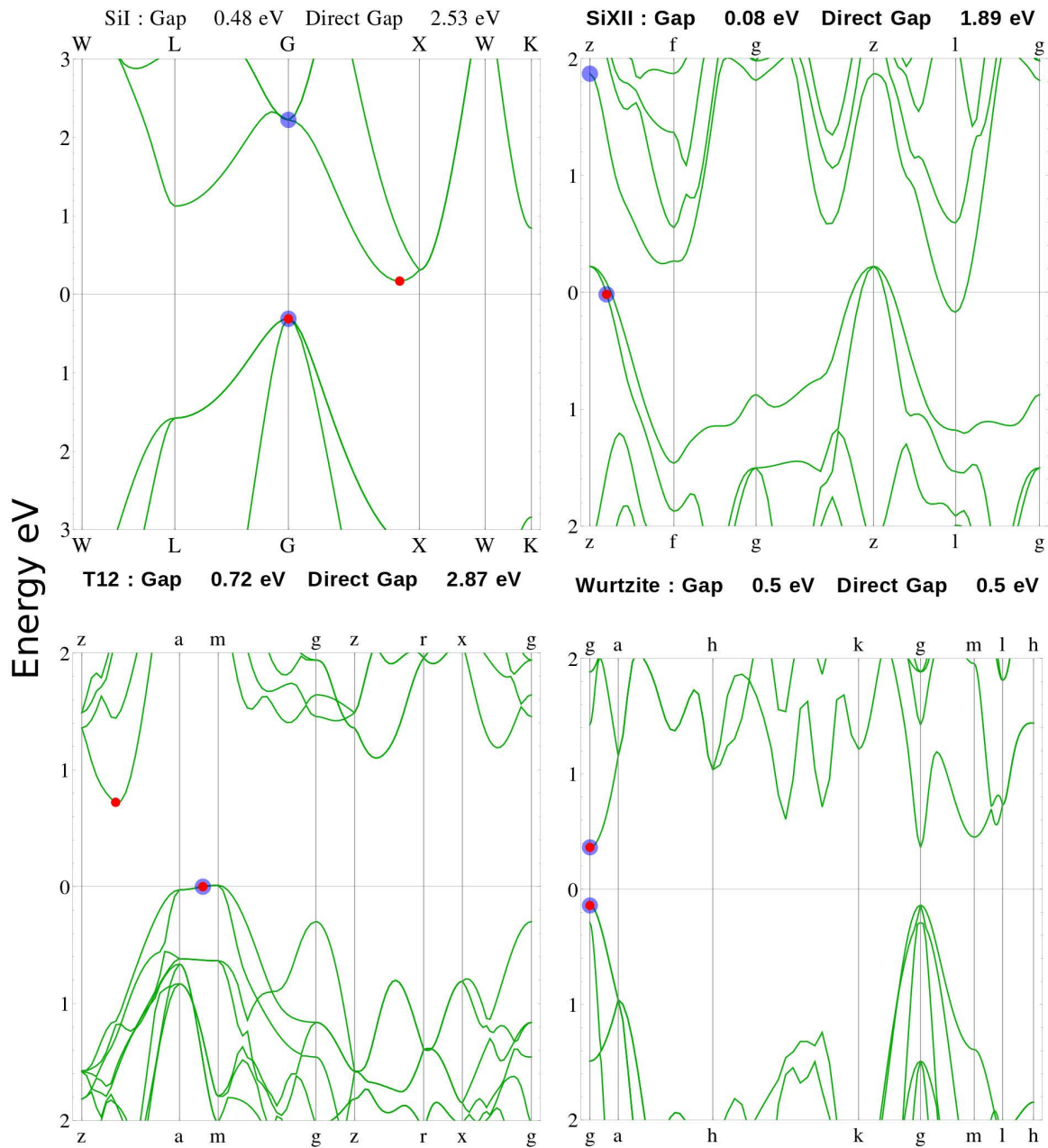


Figure 3.5: The calculated electronic band structures of silicon allotropes I, XII, T12, and Wurtzite.

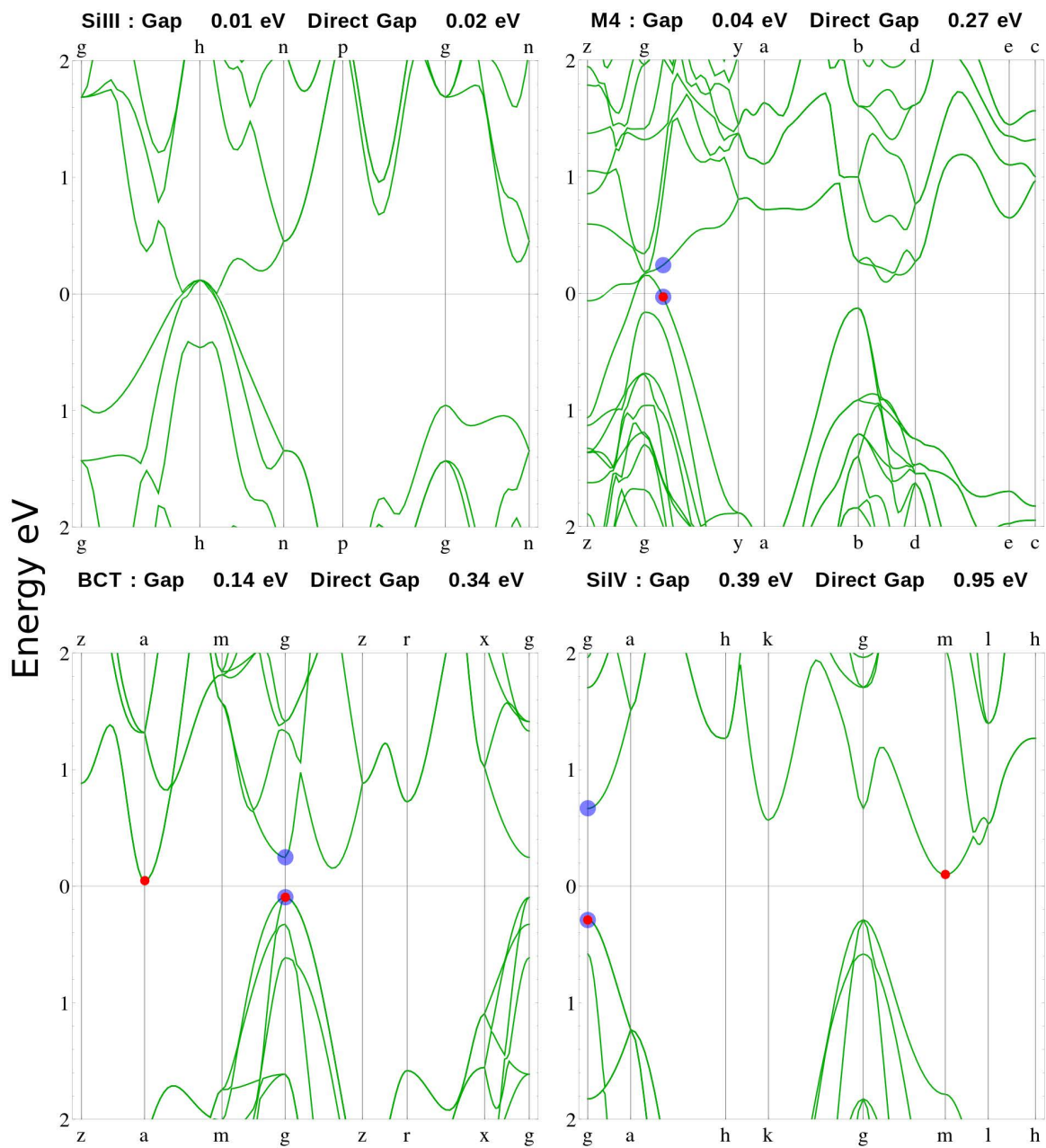


Figure 3.6: The calculated electronic band structures of silicon allotropes III, M4, BCT, and IV.

CHAPTER 4

CLATHRATE QUANTUM DOTS

In this section the clathrate quantum dots are introduced. The geometries of the quantum dots are presented using meta-structures, where each cage within a clathrate quantum dot is represented using a single atom. After the structural properties are introduced, the HOMO/LUMO gap as a function of quantum dot size, for each allotrope mentioned in Chapter 3, is reported.

4.1 Quantum Dot Structures

The geometries of the quantum dots are presented in two groups; first the relaxed clathrate quantum dot structures and second the un-relaxed quantum dots. The relaxed quantum dot structures consist only of clathrates where the un-relaxed quantum dots consist of all the silicon allotropes mentioned in Chapter 3.

4.1.1 Relaxed Clathrate Quantum Dot Structures

These quantum dot structures were relaxed using the methods and constraints mentioned in chapter 2. Each quantum dot is hydrogen passivated and contains only complete cages. As a result, all the silicon atoms at the surface of the relaxed clathrate quantum dot structures form bonds with a single hydrogen atom and three bonds with neighboring silicon atoms.

Spherical, cage-centered quantum dots with diameters ranging from 0.2 - 4.0 nm were carved from bulk clathrate crystals and were subsequently passivated with hydrogen. Each dot is therefore composed of a collection of space-filling cages, and each cage can be considered as a meta-atom. For instance, the Type-II 10-cage cluster shown in the top panel of Figure 4.1, is composed of interlocking 20-atom and 28-atom cages, but it can also be viewed more simply as the 10-meta-atom configuration in the lower panel of that figure. The meta-atom perspective allows the quantum dots to be more easily visualized and allows

their meta-point group symmetries to be identified. A complete set of 2 nm diameter dots is shown and characterized in Figure 4.2. The crystal classes considered are Si-I, clathrate Types I–VIII and H[26], and the following high-pressure Si allotropes: Si-BCT [9], Si-III [32], Si-IV [32], Si-M4 [9], Si-T12, Si- Wurtzite [33], Si-XII [32].

4.1.2 Un-relaxed Quantum Dot Structures

Along with the relaxed complete caged clathrate quantum dots in 4.1.1, several un-relaxed structures were also constructed. Because the computational cost of a geometry optimization is costly compared to that of a single energy calculation, these un-relaxed quantum dots could be much larger than the relaxed quantum dots. These un-relaxed quantum dots are composed from the relaxed bulk structures of clathrate types I through VII, type H, and 8 other silicon allotropes. The clathrate dots in this section are unlike the quantum dots in 4.1.1 because they have cages at the surface that are incomplete. This was done so that *spherical* clathrate quantum dots could be constructed from all of the clathrate types. The spherical nature of these dots is made apparent in Figure 4.3.

Along with the clathrates, quantum dots from diamond silicon, Si BCT [9], Si III [32], Si IV [32], Si M4 [9], SiT12, Si Wurtzite [33], Si XII [32] were also constructed. Like the clathrate quantum dots of this section, these quantum dots were carved from relaxed bulk structures but were never relaxed. The HOMO/LUMO gaps as a function of quantum dot size for these unrelaxed quantum dots match that of the relaxed quantum dots for sizes greater than 1.5 nm.

4.2 Spatial Confinement of the HOMO/LUMO Gap

In this section the HOMO/LUMO gap as a function of quantum dot size for Si BCT , Si III , Si IV, Si M4, SiT12, Si Wurtzite, Si XII, clathrates type I, II, III, IV, V, VI, VII, VIII, H and diamond silicon are presented.

4.2.1 HOMO/LUMO Gap

To summarize what has been covered thus far, density functional theory (DFT) was used to geometrically optimize dots less than 1.5 nm in diameter and was also used to determine the energy levels of the highest occupied and lowest unoccupied molecular orbitals (HOMO/LUMO) for both relaxed dots < 1.5 nm and unrelaxed dots between 1.5 nm and 4 nm using the methods and constraints mentioned in 2. The energy gap was taken to be the difference. The results are shown in Figure 4.4 along with those for several other Si allotropes. Two properties can be used to summarize these results, the energy gap and the sensitivity to confinement. The second property is a measure of the rate at which the energy gap increases with decreasing dot size. As is clear from the figure, having a relatively low bulk band gap is not sufficient to guarantee a low optical gap for small dots since both band gap and confinement sensitivity play a role.

The confinement sensitivity, A , to be characterized for each clathrate using the following relation:

$$E_{gap} = E_{bulk} + \frac{A}{d^{1.55}} \quad (4.1)$$

where d is the dot diameter and the exponent of 1.55 was found to give the optimal fit over all nine clathrate types. The results are summarized in Figure 4.5 where the dot types are ordered by decreasing sensitivity.

The confinement sensitivity varies from 4 to 13.86 and all clathrates are less sensitive to confinement than diamond Si. All the clathrate types have smaller HOMO/LUMO gaps as compared to diamond silicon after a certain diameter is reached. Although the sensitivity of Type VII is somewhat higher than the other allotropes, its low bulk gap allows for energy gaps that are significantly lower than the other clathrates within the 1-2 nm range. As is clear from Figure 4.4, the gaps are comparable to the high-pressure allotropes Si-III, Si-XII, and Si-M4. The properties of all systems considered are summarized in Table 3.5.

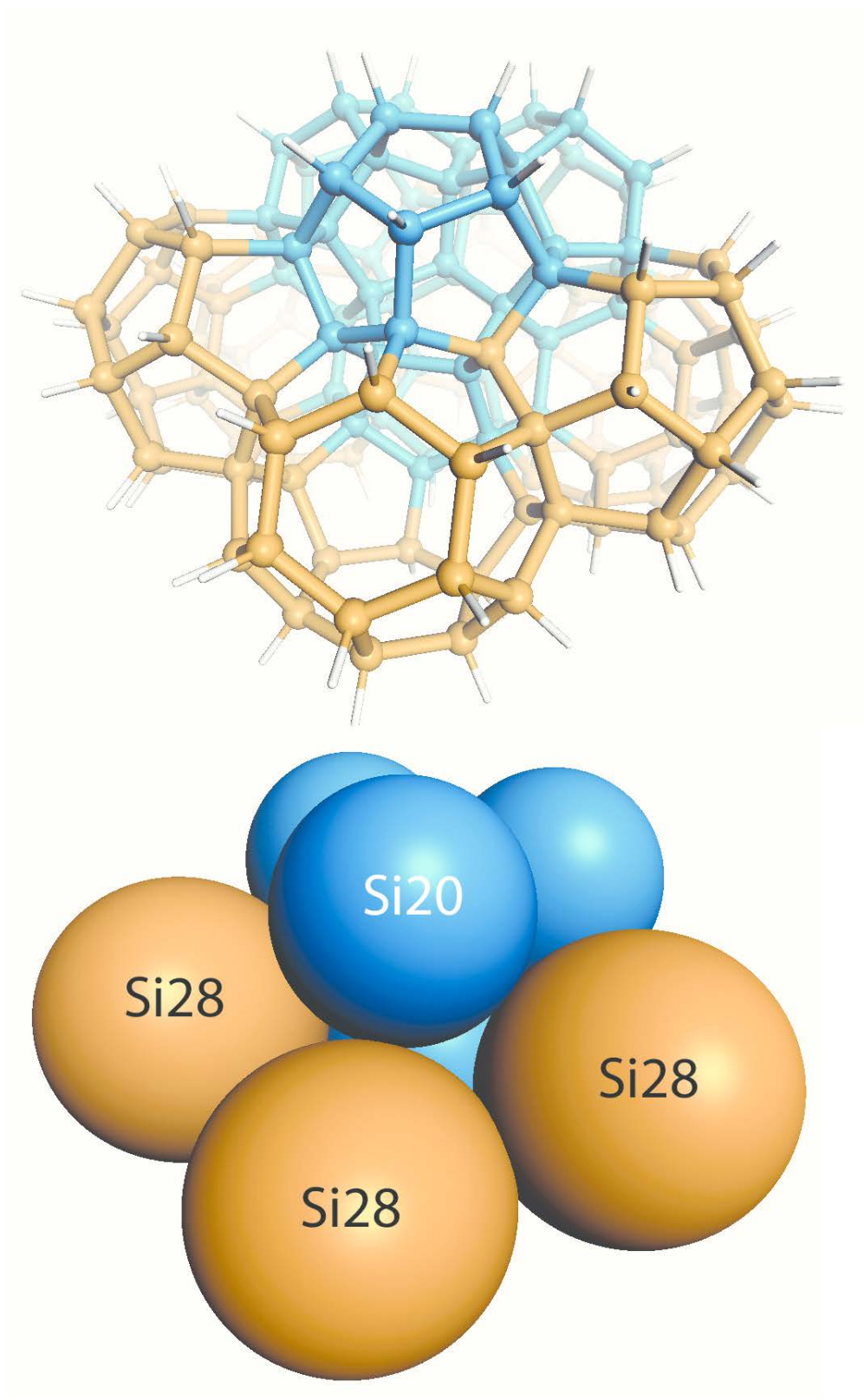


Figure 4.1: A type II clathrate quantum dot and its meta-structure.

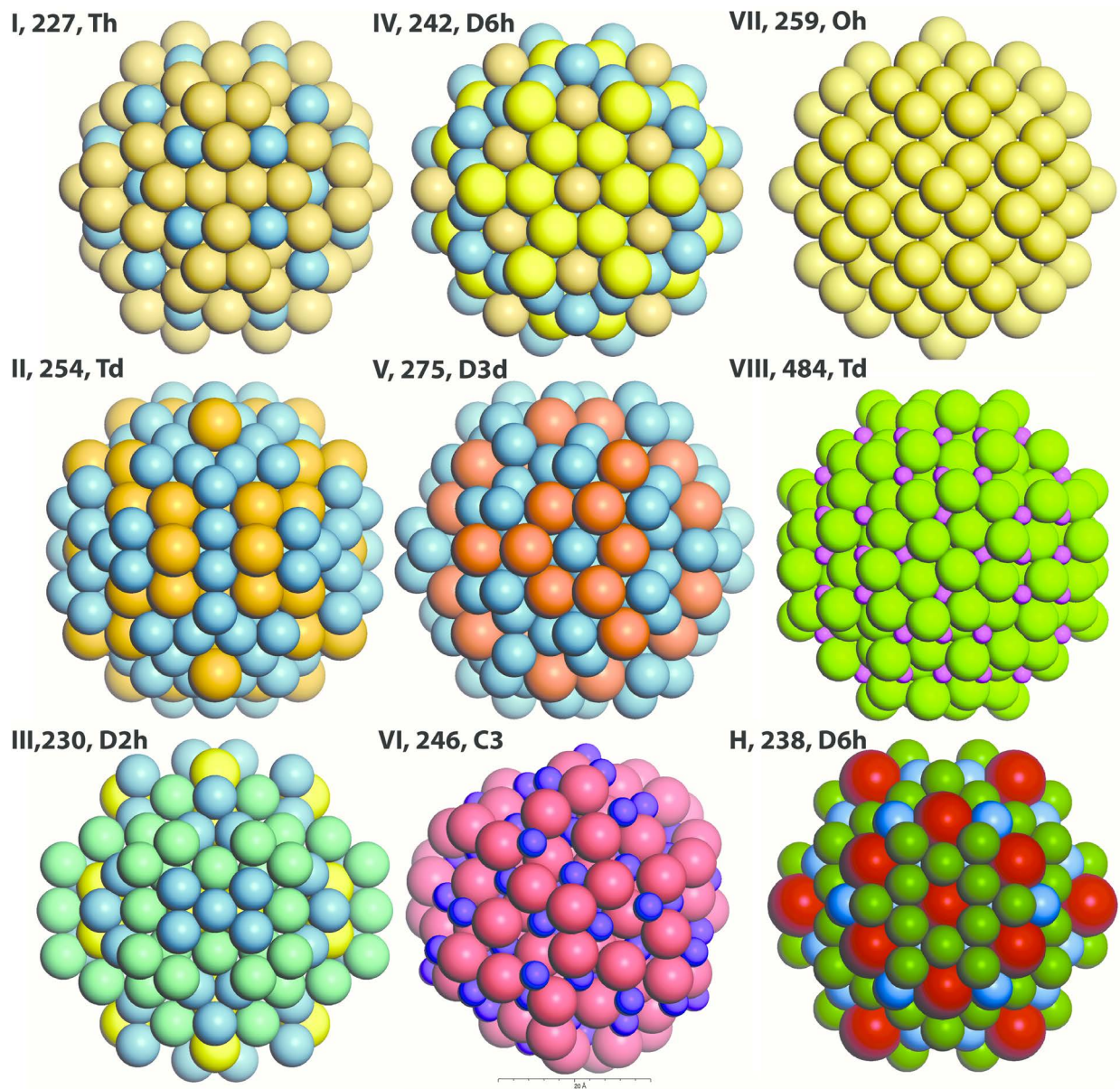


Figure 4.2: Meta-structures for several clathrate quantum dots composed of clathrates type I through VII and type H.



Figure 4.3: A series of type II silicon clathrate quantum dots composed of incomplete surface cages.

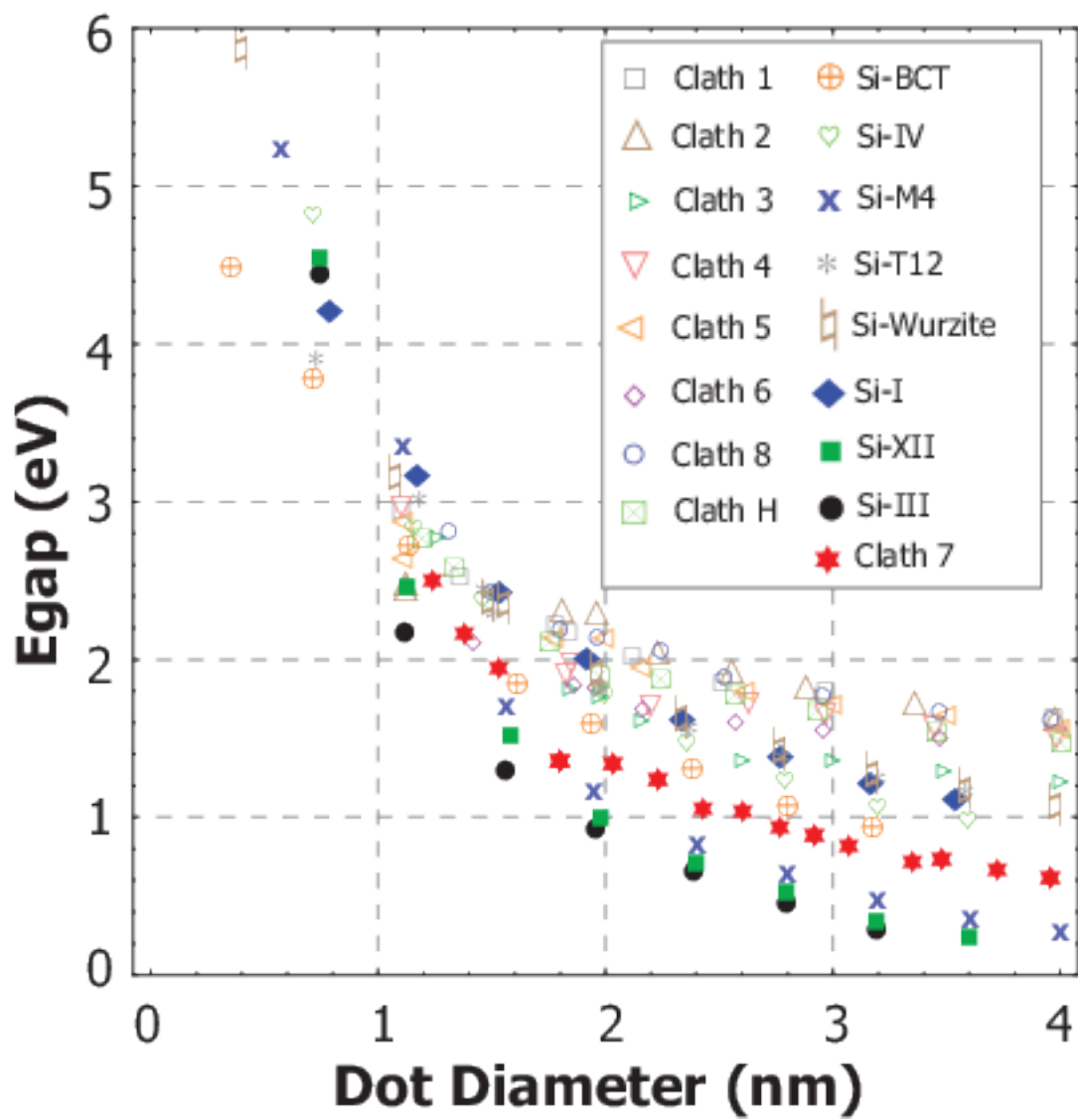


Figure 4.4: HOMO/LUMO gap as a function of unrelaxed quantum dot size for diamond silicon, clathrates type I, II, III, IV, V, VI, VII, VIII, and H.

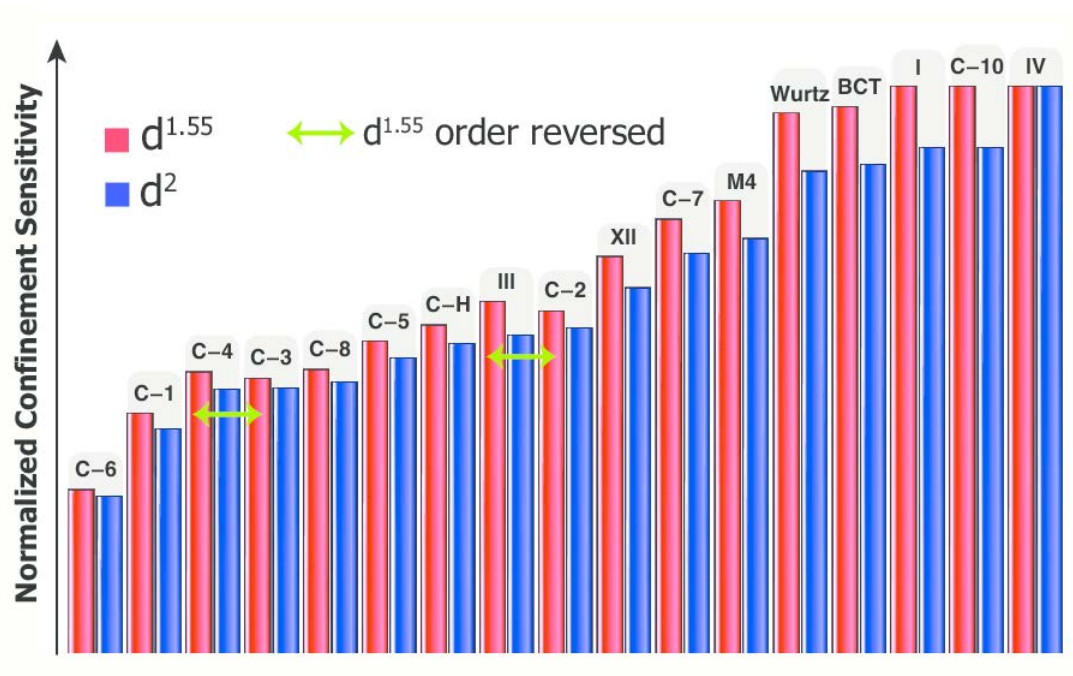


Figure 4.5: Quantum confinement sensitivity for two exponential relationships to dot diameter.

CHAPTER 5
EFFECTIVE MASS AND QUANTUM CONFINEMENT

“Science may be described as the art of systematic over-simplification” -Karl Popper

The results in 4.2, by themselves, do not explain why some clathrates are more sensitive to confinement than others. This is an important question since the consideration of clathrate quantum dots is new, and because we expect there to be a variety of additional clathrate crystals to be identified. Moreover, it would be particularly useful to be able to anticipate the optical gap of small Si dots directly from their bulk crystal properties. These issues are addressed using the effective mass approximation (EMA).

5.1 Theory

Quantum confinement is the alteration of size dependent system properties as dimensions of a system become smaller. The size dependent property investigated in this paper is the increase in the difference between the highest occupied molecular orbital (HOMO) energy and the lowest unoccupied molecular orbital (LUMO) energy as all three dimensions of the system are reduced. Within the effective mass approximation, the dispersion relation near the band edges is approximated as parabolic. All of the effects of the crystal potential are included in the effective mass, which causes the dispersion relation to deviate away from that of a free electron. The effective mass can be negative, in the case of that of a hole at the valence band edge or positive like that of the electron at the conduction band edge.

Within the single band effective mass approximation we will assume the bands to be isotropic, non-degenerate, parabolic, and occur at the Brillouin zone center. None of these assumptions are true of our materials but the end result of this analysis will give us a useful

qualitative description of the quantum confinement effect.[34] Within the single band EMA, we write the energy gap as the difference between the energy of the valence band edge and conduction band edge as, n

$$E_{gap} = \underbrace{\left(\frac{\hbar^2 k^2}{2m_c^*} + E_{bulk} \right)}_{E_{conduction}} - \underbrace{\left(\frac{\hbar^2 k^2}{2m_v^*} \right)}_{E_{valence}} \quad (5.1)$$

where E_{bulk} is the band gap of the bulk crystal and m_v and m_c are the effective masses of the valence band edge and conduction band edge respectively. During the transition from the bulk crystal to a finite structure the allowed wave vectors near band edges are assumed to remain along the parabolas defined by the effective masses but they must have values that satisfy the conditions that the wave function go to zero at the boundaries of the QD.[35] Consequently, the spacing between states along the band edges increases as the size of the system decreases.

Our next order of business is to determine the wave vector. If we assume the potential to be infinite outside our spherical quantum dot we find our wave vector to be,

$$k = \frac{\beta_{nl}}{r} \quad (5.2)$$

where β_{nl} is the nth zero of the lth order spherical Bessel function and r is the radius of the quantum dot. Upon substitution of our wave vector into the above, the energy gap is given by,

$$E_{gap} = E_{bulk} + \frac{\hbar^2 \beta_{nl}^2}{2r^2} \left(\frac{1}{m_c} + \frac{1}{|m_v|} \right) \quad (5.3)$$

Notice above that we have explicitly acknowledged the negative curvature of the valence band edge by taking the absolute value of m_v and pulling a negative out in front. We now define the reduced effective mass as,

$$\frac{1}{m^*} = \frac{m_c + m_v}{m_c m_v} \quad (5.4)$$

With the reduced effective mass we can now write E_{gap} as,

$$E_{gap} = E_{bulk} + \frac{\hbar^2 \beta_{nl}^2}{2m^* r^2} \quad (5.5)$$

The form of equation 5.5 can be found in [36, 34, 37, 38, 39] where these authors wished to explain the effects of quantum confinement of an exciton. In this work we wish to describe the HOMO/LUMO energy gap where the electron is found in the valance band state. Therefore, there is no Coulomb term in 5.5. Within this simple model, the confinement characteristics of the material is determined by the reduced effective mass and the bulk band gap of the crystal. This model also assumes that the dispersion relation remains parabolic with a constant curvature throughout the confinement process.

The consequences of applying the single band effective mass approximation to semiconductors with degenerate and non-parabolic band edges is addressed in [34, 39]. From [34],

”The above model of excitons based on electrons and holes with spherically symmetric parabolic dispersion is useful for understanding qualitatively exciton effects on optical spectra. However, it is not accurate enough for quantitative interpretation of experimental spectra in diamond- and zinc-blende-type semiconductors.”

Therefore, in our model we lose quantitative accuracy but we maintain a useful qualitative description of the confinement process. Finally, when employing the EMA to an indirect semiconductor, it is important to use the valence band and conduction band edges wherever they might be in the Brillouin zone as is done in [40]. The HOMO/LUMO states used to calculate the gap of the QD are states that originate from these band edges whether they occur at the Brillouin zone center or not. In principle, one could check this by comparing the HOMO and LUMO states in a QD to their bulk counterparts.

Now that we have established that the VBE and CBE is required to accurately described the data, we need to justify our assumption made in the model that the gap is direct and occurs at the zone center. Two common explanations are presented below.

The first argument that can be found in literature [41] is based on the Heisenberg uncertainty principle. In an indirect gap material the assistance of a phonon is needed to allow an electron to transition between the VBE and CBE. As we transition to a finite system, our uncertainty in any of the electron's positions begins to decrease. As the uncertainty in position decreases, our uncertainty in the momentum must increase due to the Heisenberg uncertainty principle. This large variance in the momentum can now afford the momentum required for electrons to transition between the VBE and CBE without the assistance of a phonon. At this point we refer to the system as "pseudo-direct". This violation of the k selection rules occur at length scales of a few nanometers [42], roughly the size of the QD's considered here. This idea is also described as the "k-space overlap of the electron and hole envelope functions" and the probability of non-phonon assisted interband transitions scales as $\frac{1}{L^6}$, where L is the size of the nanocrystal [43].

This sounds plausible but consider this, the conduction band minimum in silicon has a wave vector $\frac{\pi}{a}(1, 1, 1)$ thus the magnitude of this vector is $k = \frac{\pi\sqrt{3}}{a}$. Now the uncertainty in momentum due to confinement is given by $\Delta k = \frac{1}{2\Delta x}$. Comparison of these two values for a quantum dot of diameter 20 angstroms, suggests that the above argument does not explain the pseudo-direct behavior we observe in quantum dots of roughly this size.

$$\frac{\pi\sqrt{3}}{5.43} > \frac{2}{2(20)} \tag{5.6}$$

Where the factor of 2 on the right hand side comes from the uncertainty in the momentum of both the electron and hole.

The second argument comes from the idea of zone folding in a superlattice. A superlattice is a periodic structure consisting of multiple layers made from different materials. Because the structure is periodic, the Brillouin zone is well defined. As more layers are added to the superlattice, the conventional cell of the crystal increases and so the size of the Brillouin zone decreases. As more layers are added to a superlattice with an indirect gap, the size of the Brillouin zone changes and eventually the conduction band minimum can be folded back onto

the Γ point. This indirect to direct transition that we observe in superlattices is tempting to apply to QD's but unfortunately QD's lack translational symmetry so its application is nontrivial. A careful explanation of this idea, applied to quantum dots, is given in [40].

5.2 Comparison Between the Confinement Constant and Effective Mass

Comparison between 5.5 and 4.1 suggests a relationship between A of 4.1 and E_{gap} of 5.5 exists. To test this, the confinement data of Figure 4.4 was therefore refitted using a diameter exponent of 2.0 instead of 1.55. Because these fits were found to be most reasonable for dot diameters greater than 1.5 nanometers, only those sizes were used to generate confinement sensitivity data.

It is worth pointing out that this scaling law is different than the d^2 power law predicted by the EMA. This deviation of the results from the d^2 scaling law is well known [44, 45, 46] and is understood to be due to the nonparabolicity of the bands and quantum tunneling effects [47]. The results are expected to approach the d^2 scaling law as the dots become larger [46, 48]. Our scaling law is slightly larger than the references cited. The author believes this is due to the fact that the 1.55 value was obtained from data that consists of QD's with diameters larger than 2nm.

This EMA sensitivity parameter, $A^{(EMA)}$ is provided in Table 5.1 and Figure 5.1. The linear relation is consistent with our idealized model of the quantum dots and indicates that the bulk crystal effective mass can be used to predict confinement sensitivity for clathrate dots. When combined with the bulk crystal band gap, the optical properties of small clathrate dots can be estimated solely from bulk properties.

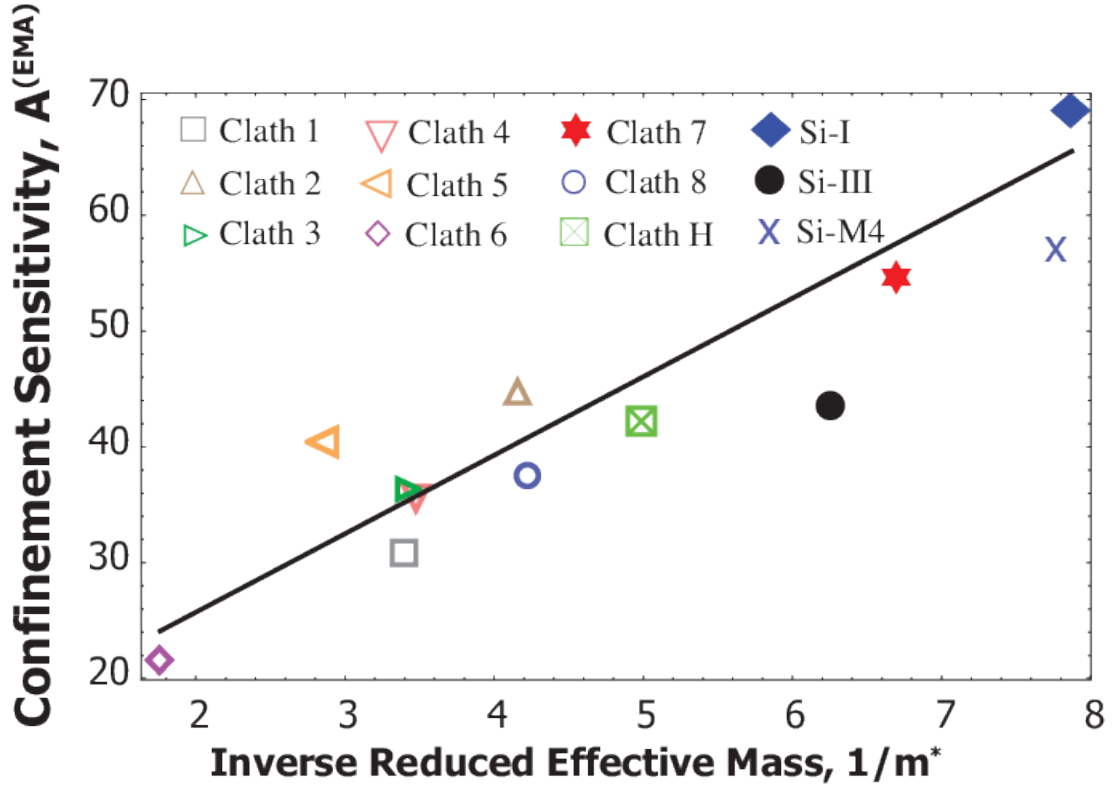


Figure 5.1: Confinement sensitivity parameter, $A^{(EMA)}$, is plotted against the inverse of the bulk, reduced effective mass, m^* .

Table 5.1: Confinement constants and reduced effective masses for diamond silicon, clathrate types I-VIII and type H.

Structure	dSi	I	II	III	IV
$A^{(EMA)} (Ha \cdot a_0^2)$	68.97	30.66	44.44	36.24	36.47
m^*	0.13	0.29	0.24	0.29	0.29
Structure	V	VI	VII	VIII	H
$A^{(EMA)} (Ha \cdot a_0^2)$	40.28	21.45	54.56	37.07	42.29
m^*	0.35	0.57	0.15	0.24	0.20

CHAPTER 6

DISCUSSION AND CONCLUSION

If the title did not give it away yet, you have reached the concluding chapter of this tired document. After the flood of figures, tables, flippant approximations and sophistries, can you remember what we set out to achieve? This work had three main goals. First, to report the spatial confinement characteristics of the HOMO/LUMO energy gap determined by first principals, density functional theory of hydrogen passivated quantum dots constructed from guest free silicon clathrate types I-VIII and type H. Second, compare these confinement characteristics to that of several other phases of silicon, namely I, BCT, III, IV, M4, T12, Wurtzite and XII. And third, the last goal, offer a reason as to why the confinement characteristics differ amongst the clathrates.

These goals were achieved through the following steps,

1. Quantum dots ranging from 0 to 4 nm in diameter from clathrate types I-VIII, H, silicon allotropes I, BCT, III, IV, M4, T12, Wurtzite, and XII were constructed.
2. Using SIESTA, the HOMO/LUMO gaps from geometrically relaxed dots smaller than 1.5 nm and unrelaxed quantum dots ranging from 1.5 to 4 nm were obtained.
3. Next the confinement sensitivity was quantified by fitting the unrelaxed data mentioned in step 2 using the relation $E_{gap} = E_{bulk} + \frac{A}{d^2}$ where A is now defined as the material's confinement sensitivity.
4. Using SIESTA again, the electronic band structures of the bulk systems were calculated to obtain the reduced effective mass for each structure.
5. The relationship between the confinement sensitivity and the reduced effective mass was found to be monotonic.

Upon completion of these steps, the first thing that was made apparent was that all the clathrate quantum dots were less sensitive to quantum confinement and had band gaps larger than that of dSi. This combination made the overall HOMO/LUMO gaps of the clathrate dots to be larger than that of dSi past a certain diameter. This was true for all clathrates except for type VII. Which for dots ranging from one to two nanometers, had HOMO/LUMO gaps similar in value to that of the high pressure phases. Leading us to believe that type VII might be a potential candidate for photo-voltaic applications.

The second useful result from this work, was the strong correlation that was obtained between confinement sensitivity and the reduced effective mass. Given only two bulk properties, the reduced effective mass and the band gap, you could predict the confinement properties of any semiconductor. As an example of the usefulness of this fact consider this, if the reduced effective mass and bulk gaps were known for each clathrate at the beginning of this work, all guest free clathrates, other than type VII, could have been ignored. The focus then would have been on guest free type VII and doped clathrates. Though this relationship between effective mass and confinement sensitivity is qualitatively useful, it is not without its flaws.

The problem with the relationship between effective mass and the confinement sensitivity is that the HOMO/LUMO gap as a function of QD size, as predicted by DFT, does not scale as d^{-2} but goes to a lesser power as the QD's become smaller. In this case the data greater than 1.5 nm was found to scale as in this case $d^{-1.55}$. By fitting the data from Figure 4.4 with the relationship $E_{gap} = E_{bulk} + \frac{A}{d^2}$, the values of A are shifted by a positive amount. This is made evident in Figure 6.1.

Along with all the simplifications made in 5.1, this overestimation of A has an additional impact on the quantitative accuracy of our model. To overcome this issue the optical gaps of each dot could be found using GW/BSE but the calculations would be computationally intensive and the end result would not be worth the time and effort. Rather than calculate values of A using GW and BSE, the author suggests that the focus of future research shift

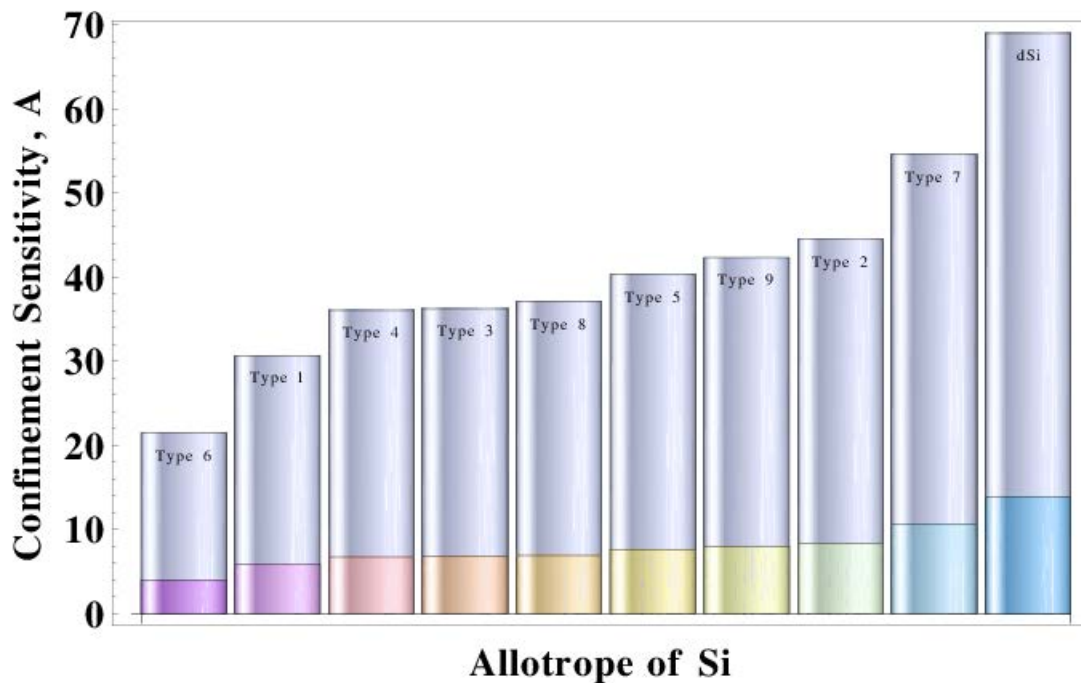


Figure 6.1: Values of the confinement sensitivity for two different power laws, d^{-2} (gray) and $d^{-1.55}$ (colored).

from A to the actual value of the HOMO/LUMO energy gap.

Type VII silicon clathrate is the only guest free clathrate in this study with gaps similar to that of the high pressure phases but it has not been observed in the laboratory. To the best of the author's knowledge only silicon clathrate types I and II have been formed in the laboratory using sodium silicide as a precursor. Sodium silicide is placed in a vacuum $\sim 10^{-6}$ Torr and heated to 375°C where it is known to decompose and form silicon clathrate.[49] Unfortunately, Figure 3.3 suggests that the type VII clathrate structure has the highest relative energy per atom. On the other hand, no unstable frequencies were found when a linear stability analysis using the DMOL software package [50] was performed on a single hydrogen passivated truncated octahedron. In regards to its synthesis in a laboratory, the author hasn't the slightest clue but an argument could be made for the right precursor that should be used. NaSi is used to make types I and II. One could predict, using DFT, a species to replace Na with such that the Si would prefer to form a type VII cage rather than the

cages found in types I and II.

A great deal of attention has been given to the extraction of Na from the type II clathrate that is formed here at the Colorado School of Mines but these dopants could prove useful when looking for small quantum dots with low optical gaps. It is known that dopants are forced to the surface in diamond silicon quantum dots. Clathrates are special because they contain interstitial sites that the dopants prefer to occupy. Unfortunately, Na has a polarizability which is too large and causes quantum dots greater than 1 nm to become metallic as the cages of the dot fill with Na. By picking guest atoms of similar size with lower polarizabilities, such as Mg and Be, quantum dots within one to two nanometers have been predicted to exhibit a significant decrease in energy gap while remaining non zero as the structure is filled by the guest atom. I predict that this juggling of polarizability and size of the guest atom within silicon quantum dots will yield small stable QDs with small optical gaps but there is no guarantee that the same quantum dots will be efficient at MEG. Transition rates will also need to be calculated.

In summary, density functional theory (DFT) has been used to quantify the bulk band gap, reduced effective mass, and HOMO/LUMO gap for nine crystal classes of clathrate quantum dots. Analogous data was also generated for diamond silicon (Si-I) as well as seven high-pressure silicon allotropes. The results show that clathrates are less sensitive to quantum confinement than Si-I while exhibiting band gaps that are both higher and lower than Si-I. A strong correlation between confinement sensitivity and reduced bulk effective mass allows the optical properties of candidate clathrate crystals to be evaluated purely from their bulk characteristics. The combination of low bulk band gap and relatively low confinement sensitivity causes the Type VII clathrate to support energy gaps comparable to those of recently studied high-pressure Si allotropes for dots with diameters in the 1-2 nm range. This suggests that Type VII clathrate quantum dots may be worthy of consideration for future optoelectronic applications, in particular as a solar cell material.

REFERENCES CITED

- [1] ZH LU, DJ LOCKWOOD, and JM BARIBEAU. QUANTUM CONFINEMENT AND LIGHT-EMISSION IN SIO₂/SI SUPERLATTICES. *NATURE*, 378(6554):258–260, NOV 16 1995.
- [2] Kai-Yuan Cheng, Rebecca Anthony, Uwe R. Kortshagen, and Russell J. Holmes. Hybrid silicon nanocrystal?organic light-emitting devices for infrared electroluminescence. *Nano Letters*, 10(4):1154–1157, 2010. PMID: 20337448.
- [3] Daniel P. Puzzo, Eric J. Henderson, Michael G. Helander, ZhiBin Wang, Geoffrey A. Ozin, and Zhenghong Lu. Visible colloidal nanocrystal silicon light-emitting diode. *Nano Letters*, 11(4):1585–1590, 2011.
- [4] Brad Malone, Jay Sau, and Marvin Cohen. Ab initio survey of the electronic structure of tetrahedrally bonded phases of silicon. *Physical Review B*, 78(3):035210, July 2008.
- [5] Ben G. Streetman and Sanjay Banerjee. *Solid State Electronic Devices*. Prentice Hall, 2000.
- [6] F. P. Bundy. Phase diagrams of silicon and germanium to 200 kbar, 1000 c. *The Journal of Chemical Physics*, 41(12):3809–3814, 1964.
- [7] R H Wentorf and J S Kasper. Two New Forms of Silicon. *Science*, 139(3552):338–339, January 1963.
- [8] J. Crain, G. J. Ackland, J. R. Maclean, R. O. Piltz, P. D. Hatton, and G. S. Pawley. Reversible pressure-induced structural transitions between metastable phases of silicon. *Phys. Rev. B*, 50:13043–13046, Nov 1994.
- [9] Fang Wu, Dai Jun, Erjun Kan, and Zhenyu Li. Density functional predictions of new silicon allotropes: Electronic properties and potential applications to li-battery anode materials. *Solid State Communications*, 151(18):1228 – 1230, 2011.
- [10] Sarah Tolbert, Amy Herhold, Louis Brus, and A Alivisatos. Pressure-Induced Structural Transformations in Si Nanocrystals: Surface and Shape Effects. *Physical Review Letters*, 76(23):4384–4387, June 1996.

- [11] Daniel C Hannah, Jihua Yang, Paul Podsiadlo, Maria K Y Chan, Arnaud Demortière, David J Gosztola, Vitali B Prakapenka, George C Schatz, Uwe Kortshagen, and Richard D Schaller. On the Origin of Photoluminescence in Silicon Nanocrystals: Pressure-Dependent Structural and Optical Studies. *Nano Letters*, 12(8):4200–4205, August 2012.
- [12] HK Poswal, N Garg, SM Sharma, E Busetto, SK Sikka, G Gundiah, FL Deepak, and CNR Rao. Pressure-induced structural phase transformations in silicon nanowires. *JOURNAL OF NANOSCIENCE AND NANOTECHNOLOGY*, 5(5):729–732, MAY 2005.
- [13] T Arguirov, T Mchedlidze, M Kittler, R Rölver, B Berghoff, M Först, and B Spangenberg. Residual stress in Si nanocrystals embedded in a SiO₂ matrix. *Applied Physics Letters*, 89(5):053111–053111–3, 2006.
- [14] A Krishna, L. L. Baranowski, A. D. Martinez, C. A. Koh, M. T. Lusk, A. C. Tamboli, and E. S. Toberer. Criteria for phase selection in silicon clathrate synthesis. *Inorganic Chemistry*, 2013, Submitted.
- [15] ED Sloan. Fundamental principles and applications of natural gas hydrates. *NATURE*, 426(6964):353–359, NOV 20 2003.
- [16] M. Beekman and G. S. Nolas. Inorganic clathrate-ii materials of group 14: synthetic routes and physical properties. *J. Mater. Chem.*, 18:842–851, 2008.
- [17] GS Nolas and GA Slack. Thermoelectric clathrates. *AMERICAN SCIENTIST*, 89(2):136–141, MAR-APR 2001.
- [18] Xun Shi, Jiong Yang, Shengqiang Bai, Jihui Yang, Hsin Wang, Miaofang Chi, James R. Salvador, Wenqing Zhang, Lidong Chen, and Winnie Wong-Ng. On the design of high-efficiency thermoelectric clathrates through a systematic cross-substitution of framework elements. *Advanced Functional Materials*, 20(5):755–763, 2010.
- [19] E. Reny, A. San-Miguel, Y. Guyot, B. Masenelli, P. Mélinon, L. Saviot, S. Yamanaka, B. Champagnon, C. Cros, M. Pouchard, M. Borowski, and A. J. Dianoux. Vibrational modes in silicon clathrate compounds: a key to understanding superconductivity. *Phys. Rev. B*, 66:014532, Jul 2002.
- [20] K Tanigaki, T Shimizu, KM Itoh, J Teraoka, Y Moritomo, and S Yamanaka. Mechanism of superconductivity in the polyhedral-network compound Ba₈Si₄₆. *NATURE MATERIALS*, 2(10):653–655, OCT 2003.

- [21] Koji Moriguchi, Shinji Munetoh, and Akira Shintani. First-principles study of $\text{si}_{34-x}\text{ge}_x$ clathrates: Direct wide-gap semiconductors in si-ge alloys. *Phys. Rev. B*, 62:7138–7143, Sep 2000.
- [22] Arnold M. Guloy, Reiner Ramlau, Zhongjia Tang, Walter Schnelle, Michael Baitinger, and Yuri Grin. A guest-free germanium clathrate. *NATURE*, 443(7109):320–323, SEP 21 2006.
- [23] Jan Gryko, Paul F. McMillan, Robert F. Marzke, Ganesh K. Ramachandran, Derek Patton, Sudip K. Deb, and Otto F. Sankey. Low-density framework form of crystalline silicon with a wide optical band gap. *Phys. Rev. B*, 62:R7707–R7710, Sep 2000.
- [24] John S. Kasper, Paul Hagenmuller, Michel Pouchard, and Christian Cros. Clathrate structure of silicon $\text{na}_8\text{si}_{46}$ and $\text{na}_x\text{si}_{136}$ ($x < 11$). *Science*, 150(3704):1713–1714, 1965.
- [25] Jan Gryko, Paul F. McMillan, Robert F. Marzke, Ganesh K. Ramachandran, Derek Patton, Sudip K. Deb, and Otto F. Sankey. Low-density framework form of crystalline silicon with a wide optical band gap. *Phys. Rev. B*, 62:R7707–R7710, Sep 2000.
- [26] Antti J. Karttunen, Thomas F. Fassler, Mikko Linnolahti, and Tapani A. Pakkanen. Structural principles of semiconducting group 14 clathrate frameworks. *Inorganic Chemistry*, 50(5):1733–1742, 2011.
- [27] Richard M. Martin. *Electronic Structure*. Cambridge University Press, New York, 2004.
- [28] David S. Sholl and Janice A. Steckel. *Density Functional Theory: A Practical Introduction*. John Wiley and Sons Inc., Hoboken, New Jersey, 2009.
- [29] Jose M Soler, Emilio Artacho, Julian D Gale, Alberto Garcia, Javier Junquera, Pablo Ordejon, and Daniel Sanchez-Portal. The siesta method for ab initio order- n materials simulation. *Journal of Physics: Condensed Matter*, 14(11):2745, 2002.
- [30] X. Gonze, J.-M. Beuken, R. Caracas, F. Detraux, M. Fuchs, G.-M. Rignanese, L. Sindic, M. Verstraete, G. Zerah, F. Jollet, M. Torrent, A. Roy, M. Mikami, Ph. Ghosez, J.-Y. Raty, and D.C. Allan. First-principles computation of material properties: the abinit software project. *Computational Materials Science*, 25(3):478 – 492, 2002.
- [31] Alexander Konchenko, Yasuo Nakayama, Iwao Matsuda, Shuji Hasegawa, Yoshiaki Nakamura, and Masakazu Ichikawa. Quantum confinement observed in ge nanodots on an oxidized si surface. *Phys. Rev. B*, 73:113311, Mar 2006.

- [32] Zhisheng Zhao, Fei Tian, Xiao Dong, Quan Li, Qianqian Wang, Hui Wang, Xin Zhong, Bo Xu, Dongli Yu, Julong He, Hui-Tian Wang, Yanming Ma, and Yongjun Tian. Tetragonal allotrope of group 14 elements. *J. of the American Chemical Society*, 134(30):12362–12365, 2012.
- [33] Yan Zhang, Zafar Iqbal, Sankaran Vijayalakshmi, and Haim Grebel. Stable hexagonal-wurtzite silicon phase by laser ablation. *Applied Physics Letters*, 75(18):2758–2760, 1999.
- [34] Peter Y. Yu and Manuel Cardona. *Fundamentals of Semiconductors*. Springer-Verlag Berlin Heidelberg, 2010.
- [35] Ying Wang and N. Herron. Nanometer-sized semiconductor clusters: materials synthesis, quantum size effects, and photophysical properties. *The Journal of Physical Chemistry*, 95(2):525–532, 1991.
- [36] Yosuke Kayanuma. Quantum-size effects of interacting electrons and holes in semiconductor microcrystals with spherical shape. *Phys. Rev. B*, 38:9797–9805, Nov 1988.
- [37] Yosuke Kayanuma. Quantum-size effects of interacting electrons and holes in semiconductor microcrystals with spherical shape. *Phys. Rev. B*, 38:9797–9805, Nov 1988.
- [38] Jingbo Li and Jian-Bai Xia. Exciton states and optical spectra in cdse nanocrystallite quantum dots. *Phys. Rev. B*, 61:15880–15886, Jun 2000.
- [39] G. T. Einevoll. Confinement of excitons in quantum dots. *Phys. Rev. B*, 45:3410–3417, Feb 1992.
- [40] Toshihide Takagahara and Kyozauro Takeda. Theory of the quantum confinement effect on excitons in quantum dots of indirect-gap materials. *Phys. Rev. B*, 46:15578–15581, Dec 1992.
- [41] E. G. Barbagiovanni, D. J. Lockwood, P. J. Simpson, and L. V. Goncharova. Quantum confinement in si and ge nanostructures. *Journal of Applied Physics*, 111(3):034307, 2012.
- [42] Nacir Tit, Zain H. Yamani, John Graham, and Ahmad Ayesh. Effects of the passivating coating on the properties of silicon nanocrystals. *Materials Chemistry and Physics*, 124(2–3):927 – 935, 2010.

- [43] D. Kovalev, H. Heckler, M. Ben-Chorin, G. Polisski, M. Schwartzkopff, and F. Koch. Breakdown of the k -conservation rule in si nanocrystals. *Phys. Rev. Lett.*, 81:2803–2806, Sep 1998.
- [44] Alex Zunger and Lin-Wang Wang. Theory of silicon nanostructures. *Applied Surface Science*, 102(0):350 – 359, 1996. Proceedings of the International Symposium on Si Heterostructures: From Physics to Devices.
- [45] Serdar Ögüt, James R. Chelikowsky, and Steven G. Louie. Quantum confinement and optical gaps in si nanocrystals. *Phys. Rev. Lett.*, 79:1770–1773, Sep 1997.
- [46] J. P. Proot, C. Delerue, and G. Allan. Electronic structure and optical properties of silicon crystallites: Application to porous silicon. *Applied Physics Letters*, 61(16):1948–1950, 1992.
- [47] Masahiko Hirao and Tsuyoshi Uda. Electronic structure and optical properties of hydrogenated silicon clusters. *Surface Science*, 306(1–2):87 – 92, 1994.
- [48] C. Delerue, G. Allan, and M. Lannoo. Theoretical aspects of the luminescence of porous silicon. *Phys. Rev. B*, 48:11024–11036, Oct 1993.
- [49] Ganesh K Ramachandran, Jianjun Dong, Jason Diefenbacher, Jan Gryko, Robert F Marzke, Otto F Sankey, and Paul F McMillan. Synthesis and x-ray characterization of silicon clathrates. *Journal of Solid State Chemistry*, 145(2):716 – 730, 1999.
- [50] B. Delley. From molecules to solids with the dmol approach. *The Journal of Chemical Physics*, 113(18):7756–7764, 2000.

APPENDIX - COMPUTATIONAL DETAILS CONTINUED

A.1 KGridCutOff

Table A.1: Values of KGridCutOff for different materials.

Sub-category	KGridCutOff (Ang) (Relaxed)	KGridCutOff (Ang) (Un-Relaxed)
dSi	35	20
Type I	40	20
Type II	28	20
Type III	37	20
Type IV	21	20
Type V	30	20
Type VI	28	20
Type VII	40	20
Type VIII	12	20
Type H	20	20
BCT	n/a	20
Si III	n/a	20
Si M4	n/a	20
Si T12	n/a	20
Si Wurtzite	n/a	20
Si XII	n/a	20
Si IV Lonsdaleite	n/a	20